

Alpha Enhancement and the Metallicity Distribution Function of Plaut's Window

Christian I. Johnson^{1,2,7}, R. Michael Rich¹, Jon P. Fulbright^{3,4}, Elena Valenti⁵, and Andrew McWilliam⁶

ABSTRACT

We present Fe, Si, and Ca abundances for 61 giants in Plaut's Window ($l=-1^\circ, b=-8.5^\circ$) and Fe abundances for an additional 31 giants in a second, nearby field ($l=0^\circ, b=-8^\circ$) derived from high resolution ($R \approx 25,000$) spectra obtained with the Blanco 4m telescope and Hydra multifiber spectrograph. The median metallicity of red giant branch (RGB) stars in the Plaut field is ~ 0.4 dex lower than those in Baade's Window, and confirms the presence of an iron abundance gradient along the bulge minor axis. The full metallicity range of our (biased) RGB sample spans $-1.5 < [\text{Fe}/\text{H}] < +0.3$, which is similar to that found in other bulge fields. We also derive a photometric metallicity distribution function for RGB stars in the ($l=-1^\circ, b=-8.5^\circ$) field and find very good agreement with the spectroscopic metallicity distribution. The radial velocity and dispersion data for the bulge RGB stars are in agreement with previous results of the *BRAVA* survey, and we find evidence for a decreasing velocity dispersion with increasing $[\text{Fe}/\text{H}]$. The $[\alpha/\text{Fe}]$ enhancement in Plaut field stars is nearly identical to that observed

¹Department of Physics and Astronomy, UCLA, 430 Portola Plaza, Box 951547, Los Angeles, CA 90095-1547, USA; cijohnson@astro.ucla.edu; rmr@astro.ucla.edu

²Department of Astronomy, Indiana University, Swain West 319, 727 East Third Street, Bloomington, IN 47405-7105, USA

³Department of Physics and Astronomy, Johns Hopkins University, Baltimore, MD 21218, USA; jfulb@skysrv.pha.jhu.edu

⁴Visiting astronomer, Cerro Tololo Inter-American Observatory, National Optical Astronomy Observatory, which are operated by the Association of Universities for Research in Astronomy, under contract with the National Science Foundation.

⁵European Southern Observatory, Karl Schwarzschild-Straße 2, D-85748 Garching bei München, Germany; evalenti@eso.org

⁶Observatories of the Carnegie Institution of Washington, Pasadena, CA, USA; andy@obs.carnegiescience.edu

⁷National Science Foundation Astronomy and Astrophysics Postdoctoral Fellow

in Baade’s window, and suggests that an $[\alpha/\text{Fe}]$ gradient does not exist between $b=-4^\circ$ and -8° . Additionally, a subset of our sample (23 stars) appear to be foreground red clump stars that are very metal-rich, exhibit small metallicity and radial velocity dispersions, and are enhanced in α elements. While these stars likely belong to the Galactic inner disk population, they exhibit $[\alpha/\text{Fe}]$ ratios that are enhanced above the thin and thick disk.

Subject headings: stars: abundances, Galactic bulge: general, bulge: Galaxy: bulge, stars: Population II

1. INTRODUCTION

The advent of multifiber spectroscopy has enabled large scale surveys of abundances and kinematics of stars in the Galactic bulge. The *Bulge Radial Velocity Assay (BRAVA)* has explored the kinematics of M giants over the inner kpc and found the dynamics to be consistent with a rapidly rotating N-body bar that leaves little room for a classical bulge component (Shen et al. 2010). These observations would argue for a relatively simple picture. However, the large scale metallicity survey by Zoccali et al. (2008) finds an abundance gradient in the outer bulge. Nominally, this would be inconsistent with a purely dynamical process such as the buckling of a massive disk, as proposed by Shen et al. (2010). Furthermore, Babusiaux et al. (2010) find that the metal-rich population appears to be more concentrated toward the plane, and that these stars also exhibit a larger velocity dispersion. Observations in multiple bulge fields will be required to sort out this complicated picture.

The distance, differential reddening, and complex populations make it difficult to quantify the internal age dispersion of the bulge. Recent studies by Zoccali et al. (2003), using a statistical disk subtraction method, and Clarkson et al. (2008), using the proper motion separation method of Kuijken & Rich (2002), argue that the bulge is $>90\%$ dominated by a stellar population comparable in age to the inner halo globular clusters. A trace population of stars brighter than the old main sequence turnoff is interpreted to be a foreground population by Feltzing & Gilmore (2000). Subsequent studies confirm this to be the foreground disk based on proper motions (Kuijken & Rich 2002) and based on subtraction of an equivalent foreground disk population (Zoccali et al. 2003).

The evidence for early, rapid formation is also supported by the detailed chemical abundances. McWilliam & Rich (1994), followed by subsequent studies (Rich & Origlia 2005; Cunha & Smith 2006; Fulbright et al. 2007; Lecureur et al. 2007; Rich et al. 2007; Alves-Brito et al. 2010; Bensby et al. 2010), found evidence that multiple α elements are enhanced

in bulge stars. This is consistent with early, rapid enrichment from Type II supernovae (SNe; e.g., Ballero et al. 2007). However, it is not clear whether the α enhancement is present only in the inner bulge, or is found over a larger volume. Shen et al. (2010) argue that there is a kinematic unity of the bulge extending from 300 to 1000 pc – essentially the entire optical bulge. Models of the deprojected photometry of the bulge are consistent with a peanut-shaped bulge dominated by a bar with its major axis aligned at $\sim 20^\circ$ from the Galactic Center.

Although there is a kinematic unity to the bulge, the picture from abundances is complex. The observed metallicity gradient requires that the enrichment history of the bulge varied as a function of location. Extragalactic analogs of the Milky Way, like NGC 4565, also have well established metallicity gradients (e.g., Proctor et al. 2000). NGC 4565 has a peanut-shaped pseudobulge that is rotationally supported like the Milky Way bulge. To date, large sample studies have not addressed whether the α enhancement observed in Baade’s Window (e.g., McWilliam & Rich 1994) and inner bulge fields (Rich et al. 2007) is also characteristic across the entire bulge, including the outer bulge fields at >1 kpc. However, we note that Lecureur et al. (2007) analyzed 5 stars at $b=-12^\circ$ (~ 1.7 kpc below the Galactic plane) and did not find a change in the abundance patterns of $[\text{O}/\text{Fe}]^1$ or $[\text{Mg}/\text{Fe}]$, compared to Baade’s Window.

Here we report a new analysis of 92 stars toward Plaut’s low extinction window ($l=0^\circ$, $b=-8^\circ$), obtained using the Hydra multifiber spectrograph on the CTIO Blanco 4m telescope, in the echelle mode. We find that this minor axis field located roughly 1 kpc from the nucleus shows a marked decline in mean metallicity compared to the $b=-4^\circ$ field of Baade’s Window. However, α elements are enhanced as they are in Baade’s Window; this argues for a common enrichment history of early, rapid formation over the full volume of the bulge extending to 1 kpc. The metallicity decline is present at the same latitude where the bulge is demonstrated to show cylindrical rotation (Howard et al. 2009; Shen et al. 2010).

The Galactic bulge at $b=-8^\circ$ is in a transition from the inner bulge into the halo. Although Zoccali et al. (2008) shows that there is a modest metallicity gradient from $b=-4^\circ$ to $b=-6^\circ$, the same study finds dramatically lower abundances at $b=-12^\circ$, but the possibility of disk contamination at this latitude is also greater. It is clear that the $b=-8^\circ$ field is an important missing link in defining the bulge metallicity gradient. Additionally, the M giants in this field have been shown by the *BRAVA* project to participate in the dynamics of the bar. We recall also that Howard et al. (2008) find no evidence for kinematic subpopulations in the

¹We make use of the standard spectroscopic notation where $[\text{A}/\text{B}] \equiv \log(\text{N}_\text{A}/\text{N}_\text{B})_\text{star} - \log(\text{N}_\text{A}/\text{N}_\text{B})_\odot$ and $\log \epsilon(\text{A}) \equiv \log(\text{N}_\text{A}/\text{N}_\text{H}) + 12.0$ for elements A and B.

radial velocity (RV) distribution of M giants, in these fields. The present dataset enables us to explore how dynamics depend on chemical composition, albeit for a more modest sample.

2. SPECTROSCOPIC OBSERVATIONS AND REDUCTIONS

The spectra for this project were obtained at Cerro Tololo Inter-American Observatory (CTIO) using the Blanco 4m telescope and Hydra multifiber spectrograph. The observations covered two separate runs spanning 2006 May 27–28 and 2007 May 19–23, and targeted the approximate spectral regions of 6000–6250, 6150–6400, 6500–6800, and 7650–7950 Å. All spectrograph setups employed the “large” 300 μm (2”) fibers, 400 mm Bench Schmidt camera, 316 line mm^{-1} Echelle grating, and 100 μm slit plate to achieve a resolving power of $R(\lambda/\Delta\lambda)\approx 25,000$. These spectrograph setups allow for abundance determinations of several light odd-Z, α , Fe-peak, and neutron-capture elements. However, the focus of this paper is on iron and the heavier α elements silicon and calcium. The remaining elemental abundances will be published in a forthcoming paper.

Two separate fields were targeted in Plaut’s low-extinction window near the bulge minor axis at (l,b)=(0°,−8°) and (−1°,−8.5°). Unfortunately, the 6100–6200 Å region, which contains most of the useful silicon and calcium lines relevant here, was only observed for the (l=−1°,b=−8.5°) field. The optical photometry for this project was obtained from observations at the Las Campanas Swope 40 inch telescope (see §3), and the infrared photometry was obtained from the Two Micron All Sky Survey Database (2MASS; Skrutskie et al. 2006).² The observing program targeted stars with V magnitudes between approximately 12.5 and 15.0 (9.5 to 12.0 in K_s), and a B–V color range from about 1.0 to 3.0 (0.6 to 1.1 in J– K_s). The observed stars for each field are shown in Figure 1.

Although we attempted to obtain an unbiased sample spanning the full color breadth of the bulge red giant branch (RGB), the final data set for each field unfortunately misses the reddest RGB stars. However, the depth along the bulge minor axis line-of-sight provides some protection against a strong metallicity bias, and a simple calculation (see §6.1) suggests our RGB sample is probably not too severely biased. Note that we have also observed 23 stars, included in the total sample of 92 stars, along the vertical sequence blueward of the RGB (filled cyan circles in Figure 1). We suspect these are foreground red clump stars that may belong to the inner Galactic disk population (see also §6).

²The 2MASS catalog can be accessed online at: <http://irsa.ipac.caltech.edu/applications/Gator/>.

All data reduction was carried out using standard tasks provided in IRAF.³ Overscan trimming and bias subtraction were applied using the *ccdproc* IRAF routine. The majority of the raw data reduction, including fiber tracing, scattered light removal, flat-field correction, wavelength calibration with ThAr comparison spectra, cosmic ray removal, background sky subtraction, and object spectrum extraction, was performed via the *dohydra* task. In all cases the reduced spectra were continuum flattened, corrected for telluric contamination, and combined. The final, co-added spectra ranged in signal-to-noise (S/N) from ~ 50 – 100 per pixel.

3. PHOTOMETRIC OBSERVATIONS AND REDUCTIONS

A set of B, V and I images for both bulge fields analyzed here spectroscopically were obtained at the Las Campanas Observatory in August 2002. We used the optical imager mounted at the Swope 40 inch telescope and equipped with the SITe#3 detector. The detector is characterized by a $0.435''$ pixel size, which provides a total field of view of $14.8' \times 22.8'$. Typical exposure times for individual images were 240, 120, and 60 seconds in the B, V, and I bands, respectively. During the observations the average seeing was ~ 1 – $1.5''$ (FWHM).

All of the raw frames have been bias and flat-field corrected by means of standard IRAF routines, using a set of sky flat-fields taken during the same night. The PSF-fitting procedure was performed independently on each image using the ALLSTAR/DAOPHOTII package (Stetson 1987). A reasonable estimate of the internal photometric accuracy ($\sigma_B \sim \sigma_V \sim \sigma_I \sim 0.03$ mag) has been obtained from the frame-to-frame rms scatter of multiple star measurements. Aperture photometry with the PHOT/DAOPHOTII routine was performed on a large sample of isolated bright stars across each frame in order to correct the PSF single-band catalogs. These have been corrected for exposure time and airmass. In particular, the atmospheric extinction coefficients were directly derived by repeated observation of Landolt (1992) standard fields at different airmasses. A final catalog listing the instrumental B, V, and I magnitudes was generated by cross-correlating the single-band catalogs, and the absolute calibration was obtained from several repeat observations of the same standard fields, finding negligible color terms. We estimate an overall uncertainty of ± 0.05 mag in the zero-point calibration for all the three bands.

³IRAF is distributed by the National Optical Astronomy Observatory, which is operated by the Association of Universities for Research in Astronomy, Inc., under cooperative agreement with the National Science Foundation.

The optical catalog was then combined with the J, H, and K_s photometry from 2MASS. This was performed in order to transform the star positions onto the 2MASS coordinate system, and provided rms residuals of $\sim 0.2''$ in both right ascension and declination.

4. SPECTROSCOPIC ANALYSIS

4.1. Model Stellar Atmospheres

The data analysis process mostly followed the procedures outlined in Fulbright et al. (2006; 2007) and Johnson & Pilachowski (2010). To briefly summarize, effective temperature (T_{eff}) and surface gravity ($\log g$) estimates were calculated primarily from V and K_s band photometry, and the metallicity ($[\text{Fe}/\text{H}]$) and microturbulence (V_t) parameters were determined spectroscopically. These values were used to generate suitable one-dimensional model atmospheres (without convective overshoot) through interpolation within the α -rich⁴ ODFNEW ATLAS9 grid (Castelli et al. 1997).⁵ Specifically, effective temperatures were calculated from the V–K color–temperature relation in Alonso et al. (1999; 2001), and surface gravities were calculated through the standard relation,

$$\log(g_*) = 0.40(M_{\text{bol.}} - M_{\text{bol.}\odot}) + \log(g_\odot) + 4[\log(T/T_\odot)] + \log(M/M_\odot), \quad (1)$$

with an assumed stellar mass of $0.80 M_\odot$ and distance of 8 kpc. The model atmosphere metallicity values were initially set at $[\text{Fe}/\text{H}] = -0.3$, and then iteratively adjusted to match the derived $[\text{Fe}/\text{H}]$ ratio from the equivalent width (EW) analysis. Similarly, the microturbulent velocity was set at 2 km s^{-1} for all stars, and then improved following the method outlined in Magain (1984) that removes trends in Fe I abundance with line strength.

Although the average color excess in Plaut’s field is $E(B-V) \approx 0.2$, differential reddening exists at about the 15% level across Hydra’s $40'$ field. Therefore, target stars were individually dereddened using the NASA/IPAC Extragalactic Database Galactic Extinction Calculator⁶, which is based on the Schlegel et al. (1998) infrared maps.

⁴Although these models assume $[\alpha/\text{Fe}] = +0.4$ for *all* α elements, we only have $[\text{Si}/\text{Fe}]$ and $[\text{Ca}/\text{Fe}]$ abundances and therefore are unable to verify the validity of this approximation. However, Fulbright et al. (2007) found that the effects of using an α -rich versus solar composition model atmosphere for a *relative* abundance analysis were small and result in an average increase of $+0.06 \pm 0.02$ dex in $[\text{Fe}/\text{H}]$, an average increase of $+0.03 \pm 0.02$ dex in $[\text{Si}/\text{Fe}]$, and an average decrease in $[\text{Ca}/\text{Fe}]$ of -0.02 ± 0.02 dex.

⁵The model atmosphere grid can be downloaded from <http://wwwuser.oat.ts.astro.it/castelli/grids.html>.

⁶The extinction calculator can be accessed at: <http://nedwww.ipac.caltech.edu/forms/calculator.html>.

Interestingly, the photometric surface gravity estimates for stars populating the vertical blue sequence seen in Figure 1 appeared too low compared to the cooler stars clearly populating the RGB. This surface gravity discrepancy suggests either that the bluer stars are closer to the Sun than 8 kpc or that a problem exists with the bolometric magnitude calculation. Therefore, we used equation 1 to compare the surface gravity values obtained when using the V magnitude bolometric correction from Alonso et al. (1999) and the K magnitude bolometric correction from Buzzoni et al. (2010). Although the bolometric magnitudes calculated from the K band will be less sensitive to reddening uncertainties, we found that the difference between the two surface gravity estimates was <0.05 dex. We interpret this result as evidence supporting the idea that the bluest stars in our sample are foreground red clump stars located $\sim 2\text{--}4$ kpc from the Sun⁷. For these stars we adopted appropriate $\log g$ values from the Padova stellar evolutionary tracks (Girardi et al. 2000), and also used the pressure sensitive 6162 Å Ca I line as a secondary guide (e.g., see Figures 2–3). Final model atmosphere parameters for all stars are provided in Table 1.

4.2. Abundance Determinations

The abundance measurement procedures for both the EW and spectrum synthesis analyses generally followed the methods outlined in Fulbright et al. (2006; 2007) and Johnson & Pilachowski (2010). Specifically, Fe I abundances were derived from a standard EW analysis where line profiles were fit with either a single Gaussian or deblended using multiple Gaussians via the interactive EW fitting code developed for Johnson et al. (2008). The Fe I line list was taken from Fulbright et al. (2006) in the available wavelength windows listed in §2 ($\sim 25\text{--}30$ lines on average). However, the individual $\log gf$ values were redetermined by forcing the EWs measured in the Arcturus atlas (Hinkle et al. 2000⁸) to match the $[\text{Fe}/\text{H}] = -0.51$ ratio derived by Fulbright et al. (2006), using the same Arcturus atmospheric parameters and α -rich ODFNEW ATLAS9 model atmosphere. The final $[\text{Fe}/\text{H}]$ abundances listed in Table 1 were determined using the derived EWs, Arcturus-based line list, and the *abfind* driver in the LTE line analysis code MOOG (Sneden 1973).

The neutral Si and Ca abundances reported here were derived from full spectrum synthe-

⁷Note that the distance estimate comes from comparing the photometric surface gravities with the theoretical gravities provided by the Padova evolutionary tracks. Note also that the few designated RGB stars lying blueward of the color cut-off in Figure 1 were relatively metal-poor, and a comparison between their photometric and “expected” surface gravities, based on the Padova tracks, suggested they were at a distance of ~ 8 kpc.

⁸The Arcturus atlas can be downloaded at: <http://www.noao.edu/archives.html>.

sis of the 6000–6250 Å region using the *synth* driver in MOOG. Sample synthetic spectrum fits to a few Si and Ca lines in metal-poor and metal-rich stars of similar T_{eff} are shown in Figure 2 for the bulge RGB sample and Figure 3 for the foreground red clump stars. Although a few additional Si and Ca lines are available in the other wavelength regions listed in §2, the 6000–6250 Å region spectra had significantly higher S/N. Unfortunately, only “Field 1” listed in Table 1 was observed in this wavelength setup, and therefore we only provide [Si/Fe] and [Ca/Fe] abundances for about two-thirds of the total sample.

The log gf values for all Si and Ca lines were determined by fitting the synthetic spectra to the Arcturus spectrum and forcing [Si/Fe]=+0.35 and [Ca/Fe]=+0.21 (Fulbright et al. 2007). Additionally, the log gf values of nearby metal lines were adjusted to match the Arcturus spectrum, using the abundances provided in Fulbright et al. (2007). Since C and N abundances were not published in Fulbright et al. (2007), we used the [C/Fe] and [N/Fe] ratios from Peterson et al. (1993) in order to set the log gf values for CN lines.

As a consistency check, we tested the effects of normalizing the log gf values to the solar spectrum and the metal-rich ([Fe/H] \approx +0.35; Gratton & Sneden 1990) giant μ Leo, which was obtained from the ELODIE archive (Moultaka et al. 2004)⁹. When comparing the abundances derived from the Arcturus based log gf values to those derived from the solar based log gf values, we found a typical systematic offsets of \sim 0.05, 0.05, and 0.10 dex for log $\epsilon(\text{Fe})$, log $\epsilon(\text{Si})$, and log $\epsilon(\text{Ca})$, respectively. Similarly, the systematic offsets when comparing the Arcturus and μ Leo based log gf scales were approximately 0.03, 0.05, and 0.10 dex for log $\epsilon(\text{Fe})$, log $\epsilon(\text{Si})$, and log $\epsilon(\text{Ca})$, respectively. In both cases the [Ca/Fe] ratios experienced larger changes than [Si/Fe] when transforming among the three abundance scales, presumably because of the significantly larger EWs of the available Ca I lines.

4.3. Abundance Error Estimates

In Table 2 we provide the calculated random ($\sigma_{\text{Rand.}}$) and systematic ($\sigma_{\text{Sys.}}$) errors for all elements analyzed in each star. The random error is defined here as the line-to-line dispersion in the derived log $\epsilon(\text{X})$ values for each element. As mentioned above, the log $\epsilon(\text{Fe})$ abundances were typically based on \sim 30 Fe I lines, and the log $\epsilon(\text{Si})$ and log $\epsilon(\text{Ca})$ abundances were based on \sim 3–5 lines each. The average $\sigma_{\text{Rand.}}$ values for Fe, Si, and Ca are 0.16 ± 0.05 , 0.07 ± 0.05 , and 0.09 ± 0.05 dex, respectively.

The systematic errors were calculated following the procedure outlined in Fulbright et al.

⁹Based on spectral data retrieved from the ELODIE archive at Observatoire de Haute-Provence (OHP).

(2007; see also McWilliam et al. 1995), and were determined using an estimated uncertainty of $T_{\text{eff}} \pm 50$ K, $\log g \pm 0.1$ cgs, $[M/H] \pm 0.16$ dex, and $V_t \pm 0.3$ km s $^{-1}$. The T_{eff} uncertainty represents the average change in our derived photometric temperatures if we assume a change in $E(B-V)$ of $\pm 15\%$, which is equal to the $E(B-V)$ dispersion across our Hydra fields. The surface gravity uncertainty represents the approximate change in the derived $\log(g)$ values if the assumed distance changes by ± 1 kpc. The model $[M/H]$ uncertainty is taken from the average line-to-line dispersion in $[Fe/H]$, and the microturbulence uncertainty was chosen by examining the spread in derived V_t values for stars of similar T_{eff} , $\log g$, and $[Fe/H]$. The average σ_{sys} values for Fe, Si, and Ca are 0.08 ± 0.02 , 0.09 ± 0.02 , and 0.08 ± 0.01 , respectively. Note that the systematic uncertainty listed in Table 2 does not include the effects of normalizing the $\log gf$ values to either the solar or μ Leo abundance scales.

A secondary issue that could affect the foreground red clump stars is whether the reddening values derived from the Schlegel et al. (1998) map are appropriate. It is possible that the estimated reddening for these stars could be systematically too large, which would lead to photometric T_{eff} estimates, and consequently $\log g$ and $[Fe/H]$ values, that are too high. Kunder et al. (2008) estimated an average $E(B-V) \approx 0.2$ in Plaut’s window from observations of bulge RR Lyrae stars, and they found a full range in color excess that spans approximately $E(B-V) = 0.1$ – 0.3 . If we take $E(B-V) = 0.1$ as a reasonable estimate of the *minimum* color excess along the Plaut field line-of-sight and assign this value to each clump star then the average corresponding change to the photometric T_{eff} estimate is about -150 K ($\sigma = 50$ K).

In Figure 4 we show plots of $\log \epsilon(\text{Fe}) - \langle \log \epsilon(\text{Fe}) \rangle$ versus excitation potential for all lines measured in all of the red clump stars, using our adopted T_{eff} values and a scale adjusted by -150 K. Ideally, plots such as Figure 4 should exhibit no slope if the adopted temperatures are correct, and the trend seen when using our adopted temperature scale indicates the red clump T_{eff} values employed here are suitable. It is clear that systematically lowering the temperatures by 150 K produces a significantly non-zero slope, and thus supports our claim that the Schlegel et al. (1998) reddening values are an appropriate choice for the red clump stars. Note that we can also reject the idea that the red clump stars are significantly less reddened from simple geometry. We estimate these stars to be located ~ 2 – 4 kpc from the Sun and thus ~ 300 – 600 pc below the Galactic plane. However, it is likely that most of the line-of-sight dust is contained within roughly ± 100 pc of the Galactic plane (e.g., Marshall et al. 2008). This suggests that the majority of the line-of-sight reddening occurs in front of the red clump stars, and therefore both the bulge and foreground red clump stars should experience similar amounts of reddening.

4.4. Radial Velocity Determinations

Radial velocity measurements were performed using the IRAF task *fxcor* to calculate the Fourier cross-correlation and *rvcor* to calculate the heliocentric correction. All program stars were measured against the same high resolution, high S/N Arcturus atlas used in the abundance analysis, but the Arcturus template spectrum was smoothed and rebinned to match Hydra’s resolution. The radial velocities were determined from the 6150–6400 Å window because it contains a large number of absorption lines and was observed for all target stars. The final radial velocities for each star are listed in Table 1, and typical measurement uncertainties reported by *fxcor* are $\sim 1 \text{ km s}^{-1}$.

5. PHOTOMETRIC ABUNDANCE ANALYSIS

Although we obtained optical photometry for both bulge fields, here we only provide a photometric abundance analysis for a field centered at $(l,b)=(-0.89^\circ, -8.45^\circ)$, which includes stars in the spectroscopic field centered at $(l,b)=(-1^\circ, -8.5^\circ)$. In order to derive a metallicity distribution function for this field we have adopted an approach similar to that described in Bellazzini et al. (2003). We compared the observed color-magnitude diagram with the empirical grid of cluster RGB ridge lines in the $[M_k, (V-K)_0]$ plane, which were carefully selected from the sample of Valenti et al. (2004a) to cover a wide metallicity range. A photometric metallicity estimate for each star is then obtained from its color by interpolating within the grid of RGB templates.

The top panel of Figure 5 shows the result of the transformation of the observed color-magnitude diagram into the absolute plane. We adopted a distance modulus of $(m-M)_0=14.47$, as measured by McNamara et al. (2000) using the RR Lyrae and δ Scuti variables in the Optical Gravitational Lensing Experiment (OGLE) survey, and a reddening $E(B-V)=0.20$, obtained by averaging the most recent extinction estimates across the Bulge (e.g., Schlegel et al. 1998; Popowski et al. 2003). The top panel of Figure 5 also includes the grid of RGB fiducial ridge lines adopted from Valenti et al. (2004a), along with the corresponding metallicity. For empirical templates we selected the Galactic globular clusters M 92, NGC 6752, NGC 288, 47 Tuc, NGC 6440, NGC 6528, and the old open cluster NGC 6791, in order to cover the widest metallicity range with suitably fine steps. In particular, NGC 6791 is currently believed to be one of the most massive ($>4000 M_\odot$; Kaluzny & Uldaski 1992), metal-rich ($[Fe/H]\sim+0.35$; Origlia et al. 2006), and oldest ($\sim 6\text{--}12 \text{ Gyr}$; Kaluzny & Uldaski 1992; Carney et al. 2005) open clusters in the Galaxy. This makes NGC 6791 an ideal template for the super-solar metallicity regime, and permitted full coverage from $-2.16\leq[Fe/H]\leq+0.35$ while avoiding major extrapolation beyond solar metallicity.

Unfortunately, the properties of the final metallicity distribution derived from similar procedures to the one used here can be sensitive to the choice of the template RGB grid used in the analysis. All previous studies deriving metallicity distribution functions from RGB colors have employed their own custom-made recipe and reference grid. Some authors adopt purely empirical, or alternatively purely theoretical grids, while others have adopted a mixture of both, using globular cluster data to set the zero-point of a given set of theoretical models or adding suitable calibrated isochrones to empirical templates in order to cover the missing metallicity range. Although the main results are probably independent of these choices, there is little doubt that the shape and other properties of the derived metallicity distribution functions are strongly affected by the details of the analysis, especially in the high metallicity regime. Here we use a pure *empirical* approach, and the accuracy of our results depend mainly on observable quantities (e.g., photometric and spectroscopic data; reddening estimates), whose errors can be understood and minimized to some extent. The use of theoretical models would be easier and more precise in principle, as the grid can be uniformly sampled. However, theoretical models still lack a proper calibration with suitable empirical templates at super-solar metallicities.

In this work the metallicity distribution function has been computed for stars within the dashed box shown in the top panel of Figure 5. We determined the luminosity and color limits primarily to avoid contamination, but also note that the RGB-tip region is more sensitive to $[\text{Fe}/\text{H}]$ differences than the lower RGB. A lower luminosity limit was set at $M_K \leq 4.5$ in order to retain the region of the RGB with the highest sensitivity to metallicity variations and to avoid contamination by red clump stars. This choice also avoids the inclusion of asymptotic giant branch (AGB) clump stars, which are predicted to lie at $M_K \sim -2.7$ (Salasnish et al. 2000; Pietrinferni et al. 2004). In this way, the most populated region of the AGB is excluded and we can be confident that only a marginal fraction of AGB stars may contaminate our sample. The upper luminosity limit was set at the RGB-tip, as derived by Valenti et al. (2004b), to avoid the inclusion of possible bright AGB stars belonging to younger populations. Finally, the blue color limit was set at $(V-K)_0 \geq 2.8$ to further minimize contamination from AGB and younger stars. The final metallicity distribution function for the observed field, based on 90 stars, is shown in the bottom panel of Figure 5.

6. RESULTS AND DISCUSSION

6.1. Spectroscopic Metallicity and Radial Velocity Distributions

Although the bulge has long been known to exhibit a broad metallicity range (e.g., Nassau & Blanco 1958), the Zoccali et al. (2008) study was the first to quantify the shape of the metallicity distribution function at multiple Galactic latitudes with high resolution spectroscopy. Their analysis showed that, at least along the minor axis beyond $b=-4^\circ$, a radial metallicity gradient was present such that the average composition decreased from $[\text{Fe}/\text{H}]\approx 0$ at $b=-4^\circ$ to $[\text{Fe}/\text{H}]\approx -0.3$ at $b=-12^\circ$. Figure 6 shows our derived metallicity distribution function in relation to the Zoccali et al. (2008) sample. The new Plaut field data confirm the existence of a minor axis metallicity gradient. We find that the median metallicity of all stars (including RGB and clump) at $b=-8^\circ$ is approximately a factor of two lower ($[\text{Fe}/\text{H}]=-0.28$) than the median metallicity of Baade’s window ($b=-4^\circ$; $[\text{Fe}/\text{H}]=+0.04$), and is also >0.1 dex lower than the median metallicity at $b=-6^\circ$ ($[\text{Fe}/\text{H}]=-0.17$). The discrepancy is slightly larger if only the stars lying along the bulge RGB in Figure 1 are included. This decreases the median metallicity in Plaut’s field to $[\text{Fe}/\text{H}]=-0.40$. Interestingly, the median metallicity at $b=-12^\circ$ ($[\text{Fe}/\text{H}]=-0.28$) is essentially the same as, or even slightly higher than, the Plaut field metallicity. This may suggest that the composition gradient levels off or becomes more shallow along the minor axis at distances $\gtrsim 1$ kpc from the Galactic center.

As mentioned in §2 and evident in Figure 1 there is likely an observational bias in our derived metallicity distribution functions. Although the distribution functions are quite similar between the two target fields (see Figure 6), neither case samples the full color range of the bulge RGB. However, the combined RGB sample shown in Figure 6 exhibits a full $[\text{Fe}/\text{H}]$ range of ~ -1.5 to $+0.3$, which is nearly identical to previous bulge observations (e.g., Rich et al. 1988; Zoccali et al. 2008). Furthermore, simply dividing the RGB samples in half by $(J-K_s)_0$ color reveals that the average and median $[\text{Fe}/\text{H}]$ differences are <0.10 dex between the redder and bluer stars. Note that the same result is found if instead one divides the samples by fitting a line through the observed RGB stars on the color–magnitude diagram and compares the average and median $[\text{Fe}/\text{H}]$ ratios for stars lying above (brighter and bluer) and below (dimmer and redder) the best–fit line. We also show in Figure 6 that the derived metallicity distribution function is qualitatively in agreement with the simple, one–zone closed box enrichment model (e.g., Mould 1984; Rich 1990), which has been shown to be true in other bulge fields as well (e.g., Zoccali et al. 2003; 2008). While these observations suggest that our sample is not seriously biased toward the metal–poor end, it is likely that the most metal–rich stars are slightly underrepresented here. In Figure 7 we directly compare the metallicity distribution functions derived from spectroscopy (limited color range) and photometry (full color range) and find that both distributions

agree reasonably well in shape, median metallicity ($[\text{Fe}/\text{H}]_{\text{spec.}}=-0.43$; $[\text{Fe}/\text{H}]_{\text{phot.}}=-0.34$), metallicity dispersion ($\sigma_{\text{spec.}}=0.42$; $\sigma_{\text{phot.}}=0.49$), and metallicity range ($-1.5 \lesssim [\text{Fe}/\text{H}] \lesssim +0.5$). Note also that both the photometric and spectroscopic metallicity distributions find a paucity of stars with $[\text{Fe}/\text{H}] < -1.5$, in agreement with the Zoccali et al. (2008) survey.

In Figure 8 we plot both the raw radial velocity distributions at $b=-8^\circ$ and the radial velocity dispersions binned by $[\text{Fe}/\text{H}]$ in 0.5 dex increments. We also include the metallicity binned velocity dispersion data from Babusiaux et al. (2010), which provide data at $b=-4^\circ$, -6° , and -12° . The median radial velocities and velocity dispersions measured here are in reasonable agreement with the *BRAVA* M giant analysis of Plaut’s field (Howard et al. 2009). If all stars in our sample are included then the median radial velocity is $\text{RV}=+2 \text{ km s}^{-1}$ ($\sigma=89 \text{ km s}^{-1}$), which is similar to the *BRAVA* results of $\langle V_{\text{GC}} \rangle \approx -20 \text{ km s}^{-1}$ ($\sigma \approx 90 \text{ km s}^{-1}$). However, if only the bulge RGB stars are included then both the median radial velocity and dispersion increase to $\text{RV}=+9 \text{ km s}^{-1}$ ($\sigma=101 \text{ km s}^{-1}$). Fortunately, the choice of whether to include the red clump stars, which exhibit a much lower velocity dispersion ($\sigma=33 \text{ km s}^{-1}$; see Figure 8) has little effect on the general shape of the Plaut field velocity dispersion profile as a function of $[\text{Fe}/\text{H}]$.

In either case there is a clear decrease in velocity dispersion with increasing metallicity. This is similar to what Babusiaux et al. (2010) found at $b=-12^\circ$, but appears quite different from the $b=-6^\circ$ field, which exhibits no correlation with metallicity, and especially the $b=-4^\circ$ field where the most metal-rich stars appear to have the highest velocity dispersion. Furthermore, the velocity dispersions found here and in the *BRAVA* survey are at least $20\text{--}40 \text{ km s}^{-1}$ larger than those predicted by the Zhao (1996) and Fux (1999) models, but the difference is $<20 \text{ km s}^{-1}$ compared with the recent Shen et al. (2010) model. We caution the reader that the most metal-poor and metal-rich bins in our dataset contain <10 stars each, and additional observations may alter the velocity dispersion profile. However, if the metallicity dependent velocity dispersion trends seen in the $b=-8^\circ$ and -12° fields are robust then we might expect the inclusion of more metal-rich stars to lower the overall observed velocity dispersion to be in better agreement with model predictions.

In addition to the 69 RGB stars we also serendipitously observed 23 stars that appear to be mostly well separated in color from the bulge giant branch (see Figure 1). Similar stars along this vertical blue sequence in other bulge fields have been tentatively identified as disk red clump stars (e.g., Zoccali et al. 2003; Vieira et al. 2007; Rangwala et al. 2009), and the Besancon model¹⁰ (Robin et al. 2003; 2004) indicates that these stars should be mostly intermediate age ($\sim 2\text{--}7 \text{ Gyr}$) thin disk stars with a median $[\text{Fe}/\text{H}] \sim +0.1$, which is

¹⁰The Besancon model can be accessed at: <http://model.obs-besancon.fr/>.

comparable to our derived $[\text{Fe}/\text{H}]=+0.05$. In addition to being separated in color, these stars appear to have three interesting characteristics: (1) a similar median radial velocity to the RGB population but a velocity dispersion that is ~ 3 times smaller, (2) a significantly higher median metallicity than the bulge and thick disk giants, and (3) noticeably enhanced $[\alpha/\text{Fe}]$ ratios (see §6.2).

It is possible that the smaller velocity dispersion of these red clump stars may be due to the small sample size, and a two sided Kolmogorov–Smirnov (KS) test (Press et al. 1992) between the RGB and clump populations is unable to strongly reject the null hypothesis that these two groups are drawn from the same parent distribution. To further test this we ran a simple bootstrap analysis with 10^6 trials that randomly selected 23 velocities from the RGB sample and measured the radial velocity dispersion. We found that there is approximately a 0.004% chance that 23 RGB stars chosen at random would produce a velocity dispersion less than or equal to the red clump dispersion (33 km s^{-1}). However, this probability increases to $\sim 6\%$ at the 2σ level (66 km s^{-1}).

The metallicity distribution function appears somewhat less ambiguous. A two sided KS test rejects the null hypothesis that the RGB and clump $[\text{Fe}/\text{H}]$ distributions were drawn from the same parent population at the 99% level. However, the same test does not rule out that the clump and thin disk stars may share similar RV and $[\text{Fe}/\text{H}]$ distributions (see also §6.3). Future observations with large sample sizes will be needed to fully investigate the true nature of these clump stars.

6.2. Alpha Element Enhancement

The consistent overproduction of α elements relative to the solar α/Fe ratio in stellar populations is generally regarded as an indicator of rapid ($\lesssim 2 \times 10^7$ years) chemical enrichment associated with Type II SNe (e.g., Tinsley 1979; Matteucci & Brocato 1990). Furthermore, it is believed that the onset of Type Ia SNe, which occurs on timescales $> 5 \times 10^8$ years, drives the $[\alpha/\text{Fe}]$ ratio downward because of the copious production of Fe-peak elements (e.g., Yoshii et al. 1996; Nomoto et al. 1997). While the downturn in the $[\alpha/\text{Fe}]$ trend occurs near $[\text{Fe}/\text{H}] \approx -1$ for the thin disk (e.g., Bensby et al. 2003; Reddy et al. 2003; Brewer & Carney 2006), the thick disk and bulge appear to retain α -enhanced stars up to $[\text{Fe}/\text{H}] \approx -0.3$ (e.g., Fulbright et al. 2007; Alves-Brito 2010). This suggests that the thick disk and bulge experienced much more rapid and efficient star formation, but may also be an indication of other differences related to parameters such as the initial mass function, gas inflow/outflow, and the binary fraction.

Although past studies have shown that bulge stars generally maintain a high $[\alpha/\text{Fe}]$ ratio, relative to the thin disk trend, at low Galactic latitudes (McWilliam & Rich 1994; Rich & Origlia 2005; Cunha & Smith 2006; Fulbright et al. 2007; Lecureur et al. 2007; Rich et al. 2007; Alves–Brito et al. 2010; Bensby et al. 2010), we provide here the first detailed analysis of stars approximately 1 kpc from the Galactic center. In Figure 9 we plot our derived $[\text{Si}/\text{Fe}]$, $[\text{Ca}/\text{Fe}]$, and $[\alpha/\text{Fe}]$ ¹¹ ratios as a function of $[\text{Fe}/\text{H}]$, and compare our results to the thin and thick disk trends as well as Baade’s window. We find that the $[\alpha/\text{Fe}]$ versus $[\text{Fe}/\text{H}]$ trends in the Plaut field are nearly indistinguishable from those in Baade’s window. In other words, we find that no strong gradient in $[\alpha/\text{Fe}]$ exists between $b=-4^\circ$ and -8° , despite the clear presence of a metallicity gradient. This suggests that the bulge chemical enrichment process acted rapidly and with surprising uniformity over a very large volume.

Recent analyses have argued that the thick disk and bulge may share similar $[\alpha/\text{Fe}]$ enhancements despite exhibiting clear differences in their metallicity distribution functions (Meléndez et al. 2008; Alves–Brito et al. 2010; Bensby et al. 2010; Ryde et al. 2010). While we find that the $[\text{Si}/\text{Fe}]$, $[\text{Ca}/\text{Fe}]$, and $[\alpha/\text{Fe}]$ ratios are generally enhanced by ~ 0.2 dex in bulge giants compared to thick disk giants (and dwarfs), this enhancement is not extraordinarily different than the combined measurement uncertainty and choice of abundance normalization scale mentioned in §4. Interestingly, both the thick disk and bulge appear to show similar declines in the $[\alpha/\text{Fe}]$ ratio at $[\text{Fe}/\text{H}]\approx -0.3$. However, it remains to be seen whether these two populations are truly distinct in their α element composition. Fortunately, the difference in the $[\alpha/\text{Fe}]$ ratios between bulge and thin disk stars is much clearer, especially near the median metallicity of the Plaut field. However, the two populations may appear to merge with $[\alpha/\text{Fe}]\approx 0$ at $[\text{Fe}/\text{H}]\gtrsim 0$. More Plaut field observations at $[\text{Fe}/\text{H}]>0$ are needed to confirm the exact nature of the $[\alpha/\text{Fe}]$ trend at the highest bulge metallicities.

Finally, in addition to the red clump stars shown in Figure 1 exhibiting a high average metallicity, relatively small metallicity dispersion, and a low velocity dispersion, these stars appear to be just as enhanced in α elements as the bulge RGB stars. We attribute the larger scatter in $[\text{Si}/\text{Fe}]$, $[\text{Ca}/\text{Fe}]$, and $[\alpha/\text{Fe}]$ to be due mostly to surface gravity uncertainties. Nevertheless, these are likely foreground stars located $\sim 2\text{--}4$ kpc away, and their projected location at $b=-8^\circ$ places them $\sim 300\text{--}600$ pc below the Galactic plane. However, the typical metallicities of these stars are much higher than most of the thick disk, and the $[\alpha/\text{Fe}]$ enhancement suggests they do not share a similar composition with the more metal-rich thick and thin disk stars (see Figure 9). There is also the possibility that these stars, especially given their interesting kinematic and chemical composition properties, belong to a

¹¹Note that the $[\alpha/\text{Fe}]$ value is the average of the $[\text{Si}/\text{Fe}]$ and $[\text{Ca}/\text{Fe}]$ ratios.

stellar stream, but unfortunately our current dataset is unable to test this scenario without additional observations.

6.3. Possible RGB and Red Clump Contamination

Since the bulge RGB stars analyzed here lie near the center of the Galaxy, roughly 8 kpc from the Sun, and 1 kpc below the Galactic plane, any sample that is chosen purely from a color–magnitude diagram will likely contain at least some Galactic thin disk, thick disk, and halo interlopers. We first examined the likelihood of contamination by analyzing the expected number counts from each population in a theoretical color–magnitude diagram, calculated from the Besancon model, spanning the color and luminosity range of our targets. The Besancon model returned the following population breakdown for the RGB sample: 3% young (<1 Gyr) thin disk, 33% old (>1 Gyr) thin disk, 20% thick disk, 1% halo, and 43% bulge. We also ran the simulation for the red clump stars and obtained the following distribution: 1% young thin disk, 62% old thin disk, 13% thick disk, 1% halo, and 23% bulge. While the halo can be effectively ruled out as a major contaminant, based on both the $[\text{Fe}/\text{H}]$ distribution and Besancon model, the thin and thick disk populations require further analysis.

Figures 10–11 show our derived $[\text{Fe}/\text{H}]$ and RV distributions compared with those predicted by the Besancon model for the young thin disk, old thin disk, thick disk, and bulge. For the RGB sample the thin disk can be mostly ruled out as a major contaminant because the velocity and metallicity dispersions are too small, the average metallicity is too high, and the majority of the Plaut stars have $[\alpha/\text{Fe}]$ ratios that are at least a factor of two above those observed in the thin disk (see Figure 9). On the other hand, the thick disk contamination is more difficult to rule out. The thick disk appears to show a similar velocity distribution, but the median $[\text{Fe}/\text{H}]$ ratio of the Plaut field stars is ~ 0.4 dex higher than in the thick disk. Additionally, the Plaut stars extend to much higher metallicities than the thick disk distribution. However, thick disk contamination at about the 10–20% level for the more metal–poor Plaut RGB stars seems reasonable, especially given that several (~ 5 – 10) of the Plaut RGB stars with $[\text{Fe}/\text{H}] < -0.5$ exhibit $[\alpha/\text{Fe}]$ ratios that are in–line with literature thick disk giants (see Figure 9). Interestingly, the theoretical bulge velocity distribution provided by the Besancon model fits our observed data rather well, but the $[\text{Fe}/\text{H}]$ distribution is a poor fit. The model clearly overestimates the average bulge metallicity at $b = -8^\circ$, and instead predicts a distribution more similar to that seen at $b = -4^\circ$.

For the foreground red clump sample the Besancon model effectively rules out the thick disk and bulge, based on both the velocity and $[\text{Fe}/\text{H}]$ distributions. Although the average

[Fe/H] value for the model bulge is similar to the red clump sample, we have already shown that the model is likely a poor fit to the true bulge metallicity distribution at $b=-8^\circ$. The thin disk provides a decent fit for both the [Fe/H] and velocity distributions, but the $[\alpha/\text{Fe}]$ enhancements observed in the red clump stars are clearly above those observed in the thin disk (see Figure 9). This reinforces the need for more observations of these objects.

7. SUMMARY

We have determined Fe, Si, and Ca abundances for 61 stars and Fe abundances for an additional 31 stars in Plaut’s low extinction window using high resolution ($R \approx 25,000$) spectra obtained with the Hydra multifiber spectrograph at CTIO. Additionally, we have derived a metallicity distribution function from 2MASS infrared and optical photometry obtained with the Swope 40 inch telescope at Las Campanas in a nearby bulge field that is in reasonable agreement with the spectroscopic results. We find that the median [Fe/H] ratio has declined by ~ 0.4 dex from Baade’s Window at $b=-4^\circ$, and that the $b=-8^\circ$ field is part of a smoothly declining metallicity gradient. Despite a lower overall metallicity in the $b=-8^\circ$ field, the full range of derived [Fe/H] abundances is nearly identical to previous studies at $b=-4^\circ$, -6° , and -12° , with $-1.5 < [\text{Fe}/\text{H}] < +0.3$. Furthermore, the metallicity distribution at $b=-8^\circ$ is consistent with a simple model with a declining yield, due to the removal of metals by winds. The radial velocity distribution and dispersion of bulge RGB stars in the Plaut field are also in agreement with results from the *BRAVA* survey, and we find that the velocity dispersion decreases as a function of increasing metallicity, similar to what was found previously at $b=-12^\circ$.

The α element enhancements are consistent with a rapid enrichment process involving massive star SNe. While the bulge RGB stars are enhanced above the level of the thin and thick disk, the difference in $[\alpha/\text{Fe}]$ between the bulge and thick disk is smaller and may be affected by systematic offsets. However, we find that the enhancements of Si and Ca are nearly indistinguishable from those in Baade’s Window, which suggests the lack of an $[\alpha/\text{Fe}]$ gradient along the bulge minor axis despite the presence of a metallicity gradient.

A subset of our sample are candidate red clump stars that lie closer to the Sun, distributed along the line-of-sight toward the bulge. While our data are insufficient to assign a population membership to these stars, they exhibit some very interesting properties that warrant further investigation: (1) the stars are significantly more metal-rich (median [Fe/H] $\sim +0.05$) than the bulge RGB sample and exhibit a rather small [Fe/H] dispersion, (2) the mean radial velocity is similar to the bulge RGB stars but the velocity dispersion is about a factor of three smaller, and (3) these stars also have enhanced $[\alpha/\text{Fe}]$ ratios like the

bulge giants. While similar stars in bulge color–magnitude diagrams have been designated as intermediate age disk red clump stars in the past, the data suggest that their chemical composition and kinematic properties are inconsistent with belonging to either the local thin or thick disk populations.

We would like to thank the anonymous referee for a careful reading and insightful comments that led to improvement of the manuscript. We would also like to thank Mark Morris, Caty Pilachowski, and Andrea Kunder for helpful discussions, and David Reitzel for obtaining a portion of these observations. This publication makes use of data products from the Two Micron All Sky Survey, which is a joint project of the University of Massachusetts and the Infrared Processing and Analysis Center/California Institute of Technology, funded by the National Aeronautics and Space Administration and the National Science Foundation. This research has made use of NASA’s Astrophysics Data System Bibliographic Services. This research has made use of the NASA/IPAC Extragalactic Database (NED) which is operated by the Jet Propulsion Laboratory, California Institute of Technology, under contract with the National Aeronautics and Space Administration. Support of the College of Arts and Sciences at Indiana University Bloomington for CIJ is gratefully acknowledged. This material is based upon work supported by the National Science Foundation under award No. AST–1003201 to CIJ and award No. AST–0709479 to RMR.

REFERENCES

- Alonso, A., Arribas, S., & Martínez-Roger, C. 1999, *A&AS*, 140, 261
- Alonso, A., Arribas, S., & Martínez-Roger, C. 2001, *A&A*, 376, 1039
- Alves-Brito, A., Meléndez, J., Asplund, M., Ramírez, I., & Yong, D. 2010, *A&A*, 513, A35
- Babusiaux, C., et al. 2010, *A&A*, 519, A77
- Ballero, S. K., Matteucci, F., Origlia, L., & Rich, R. M. 2007, *A&A*, 467, 123
- Bellazzini, M., Cacciari, C., Federici, L., Fusi Pecci, F., & Rich, M. 2003, *A&A*, 405, 867
- Bensby, T., Feltzing, S., & Lundström, I. 2003, *A&A*, 410, 527
- Bensby, T., Feltzing, S., Lundström, I., & Ilyin, I. 2005, *A&A*, 433, 185
- Bensby, T., et al. 2010, *A&A*, 512, A41

- Brewer, M.-M., & Carney, B. W. 2006, *AJ*, 131, 431
- Buzzoni, A., Patelli, L., Bellazzini, M., Pecci, F. F., & Oliva, E. 2010, *MNRAS*, 403, 1592
- Carney, B. W., Lee, J. W. & Dodson, B. 2005, *AJ*, 129, 656
- Castelli, F., Gratton, R. G., & Kurucz, R. L. 1997, *A&A*, 318, 841
- Clarkson, W., et al. 2008, *ApJ*, 684, 1110
- Cunha, K., & Smith, V. V. 2006, *ApJ*, 651, 491
- Feltzing, S., & Gilmore, G. 2000, *A&A*, 355, 949
- Fulbright, J. P. 2000, *AJ*, 120, 1841
- Fulbright, J. P., McWilliam, A., & Rich, R. M. 2006, *ApJ*, 636, 821
- Fulbright, J. P., McWilliam, A., & Rich, R. M. 2007, *ApJ*, 661, 1152
- Fux, R. 1999, *A&A*, 345, 787
- Girardi, L., Bressan, A., Bertelli, G., & Chiosi, C. 2000, *A&AS*, 141, 371
- Gratton, R. G., & Sneden, C. 1990, *A&A*, 234, 366
- Hinkle, K., Wallace, L., Valenti, J., & Harmer, D. 2000, *Visible and Near Infrared Atlas of the Arcturus Spectrum 3727-9300 Å* ed. Kenneth Hinkle, Lloyd Wallace, Jeff Valenti, and Dianne Harmer. (San Francisco: ASP) ISBN: 1-58381-037-4, 2000
- Howard, C. D., Rich, R. M., Reitzel, D. B., Koch, A., De Propriis, R., & Zhao, H. 2008, *ApJ*, 688, 1060
- Howard, C. D., et al. 2009, *ApJ*, 702, L153
- Johnson, C. I., Pilachowski, C. A., Simmerer, J., & Schwenk, D. 2008, *ApJ*, 681, 1505
- Johnson, C. I., & Pilachowski, C. A. 2010, *ApJ*, 722, 1373
- Kaluzny, J. & Uldaski, A. 1992, *ACTA*, 42, 29
- Kuijken, K., & Rich, R. M. 2002, *AJ*, 124, 2054
- Kunder, A., Popowski, P., Cook, K. H., & Chaboyer, B. 2008, *AJ*, 135, 631
- Landolt, A. U. 1992, *AJ*, 104, 340

- Lecureur, A., Hill, V., Zoccali, M., Barbuy, B., Gómez, A., Minniti, D., Ortolani, S., & Renzini, A. 2007, *A&A*, 465, 799
- Magain, P. 1984, *A&A*, 134, 189
- Marshall, D. J., Robin, A. C., Reylé, C., Schultheis, M., & Picaud, S. 2006, *A&A*, 453, 635
- Matteucci, F., & Brocato, E. 1990, *ApJ*, 365, 539
- Meléndez, J., et al. 2008, *A&A*, 484, L21
- McNamara, D. H., Madsen, J. B., Barnes, J., Ericksen, B. F. 2000, *PASP*, 112, 202
- McWilliam, A., & Rich, R. M. 1994, *ApJS*, 91, 749
- McWilliam, A., Preston, G. W., Sneden, C., & Searle, L. 1995, *AJ*, 109, 2757
- Mould, J. R. 1984, *PASP*, 96, 773
- Moultaka, J., Ilovaisky, S. A., Prugniel, P., & Soubiran, C. 2004, *PASP*, 116, 693
- Nassau, J. J., & Blanco, V. M. 1958, *ApJ*, 128, 46
- Nomoto, K., Iwamoto, K., Nakasato, N., Thielemann, F.-K., Brachwitz, F., Tsujimoto, T., Kubo, Y., & Kishimoto, N. 1997, *Nuclear Physics A*, 621, 467
- Origlia, L., Valenti, E., Rich, R. M. & Ferraro, F. R. 2006, *ApJ*, 646, 4990
- Peterson, R. C., Dalle Ore, C. M., & Kurucz, R. L. 1993, *ApJ*, 404, 333
- Pietrinferni, A., Cassisi, S., Salaris, M. & Castelli, F. 2004, *MnSAI*, 75, 170
- Popowski, P., Cook, K. M. & Becker, A. C. 2003, *AJ*, 126, 2910
- Press, W. H., Teukolsky, S. A., Vetterling, W. T., & Flannery, B. P. 1992, Cambridge: University Press, —c1992, 2nd ed.
- Proctor, R. N., Sansom, A. E., & Reid, I. N. 2000, *MNRAS*, 311, 37
- Rangwala, N., Williams, T. B., & Stanek, K. Z. 2009, *ApJ*, 691, 1387
- Reddy, B. E., Tomkin, J., Lambert, D. L., & Allende Prieto, C. 2003, *MNRAS*, 340, 304
- Reddy, B. E., Lambert, D. L., & Allende Prieto, C. 2006, *MNRAS*, 367, 1329
- Rich, R. M. 1988, *AJ*, 95, 828

- Rich, R. M. 1990, European Southern Observatory Conference and Workshop Proceedings, 35, 65
- Rich, R. M., & Origlia, L. 2005, *ApJ*, 634, 1293
- Rich, R. M., Origlia, L., & Valenti, E. 2007, *ApJ*, 665, L119
- Robin, A. C., Reyl  , C., Derri  re, S., & Picaud, S. 2003, *A&A*, 409, 523
- Robin, A. C., Reyl  , C., Derri  re, S., & Picaud, S. 2004, *A&A*, 416, 157
- Ryde, N., et al. 2010, *A&A*, 509, A20
- Salasnish, B., Girardi, L., Weiss, A. & Chiosi, C. 2000, *A&A*, 361, 1023
- Schlegel, D. J., Finkbeiner, D. P., & Davis, M. 1998, *ApJ*, 500, 525
- Shen, J., Rich, R. M., Kormendy, J., Howard, C. D., De Propriis, R., & Kunder, A. 2010, *ApJ*, 720, L72
- Skrutskie, M. F., et al. 2006, *AJ*, 131, 1163
- Snedden, C. 1973, *ApJ*, 184, 839
- Soto, M., Rich, R. M., & Kuijken, K. 2007, *ApJ*, 665, L31
- Stetson, P. B. 1987, *PASP*, 99, 191
- Tinsley, B. M. 1979, *ApJ*, 229, 1046
- Valenti, E. Ferraro, F. R. & Origlia, L. 2004a, *MNRAS*, 351, 1204
- Valenti, E. Ferraro, F. R. & Origlia, L. 2004b, *MNRAS*, 354, 815
- Vieira, K., et al. 2007, *AJ*, 134, 1432
- Yoshii, Y., Tsujimoto, T., & Nomoto, K. 1996, *ApJ*, 462, 266
- Zhao, H. S. 1996, *MNRAS*, 283, 149
- Zoccali, M., et al. 2003, *A&A*, 399, 931
- Zoccali, M., Hill, V., Lecureur, A., Barbuy, B., Renzini, A., Minniti, D., G  mez, A., & Ortolani, S. 2008, *A&A*, 486, 177

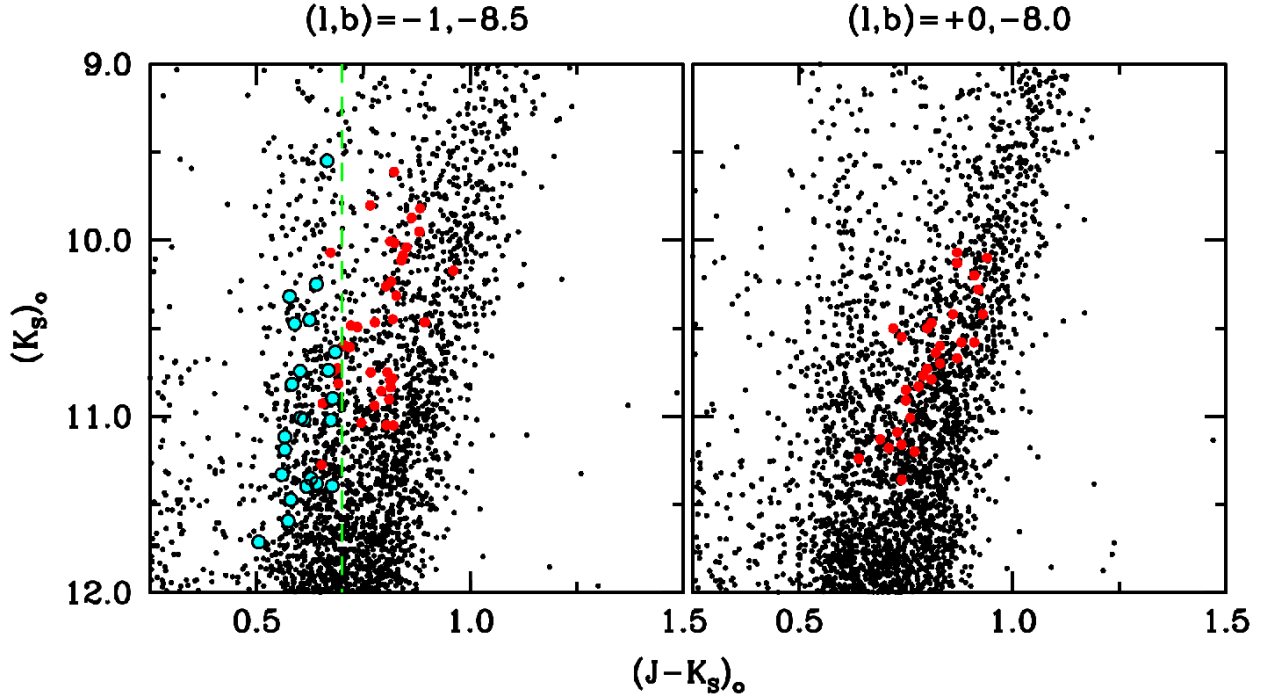


Fig. 1.— Color-magnitude diagram of Plaut’s window taken from the 2MASS database (filled black circles). The two panels indicate the stars chosen for observation in this program. The filled red circles in both panels indicate probable RGB stars belonging to the bulge population, and the filled cyan circles indicate probable foreground red clump stars. In the left panel the dashed green line indicates the approximate color cutoff used to separate the RGB and clump populations (see text for details).

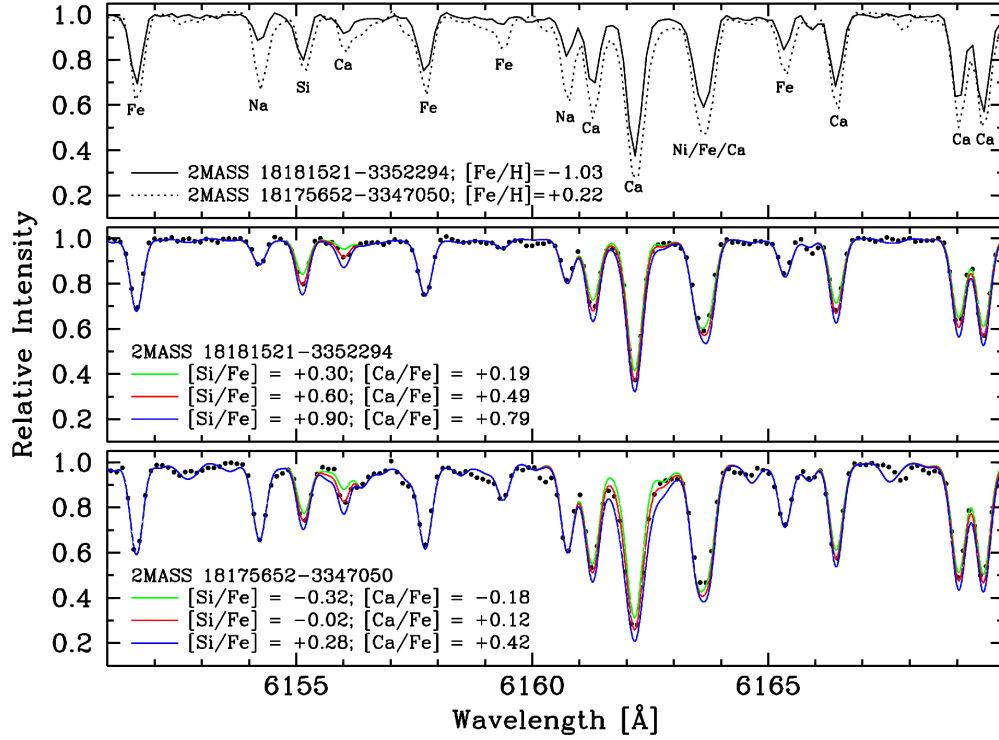


Fig. 2.— The top panel illustrates the contrasting line strengths between two stars in our bulge RGB sample with similar effective temperatures ($T_{\text{eff}} \approx 4200$ K) but different metallicities. Several key lines are identified for guidance. The middle and bottom panels show sample synthetic spectrum fits to the data with the $[\text{Si}/\text{Fe}]$ and $[\text{Ca}/\text{Fe}]$ ratios set at the best-fit values (red lines), and also altered by -0.30 dex (green lines) and $+0.30$ dex (blue lines).

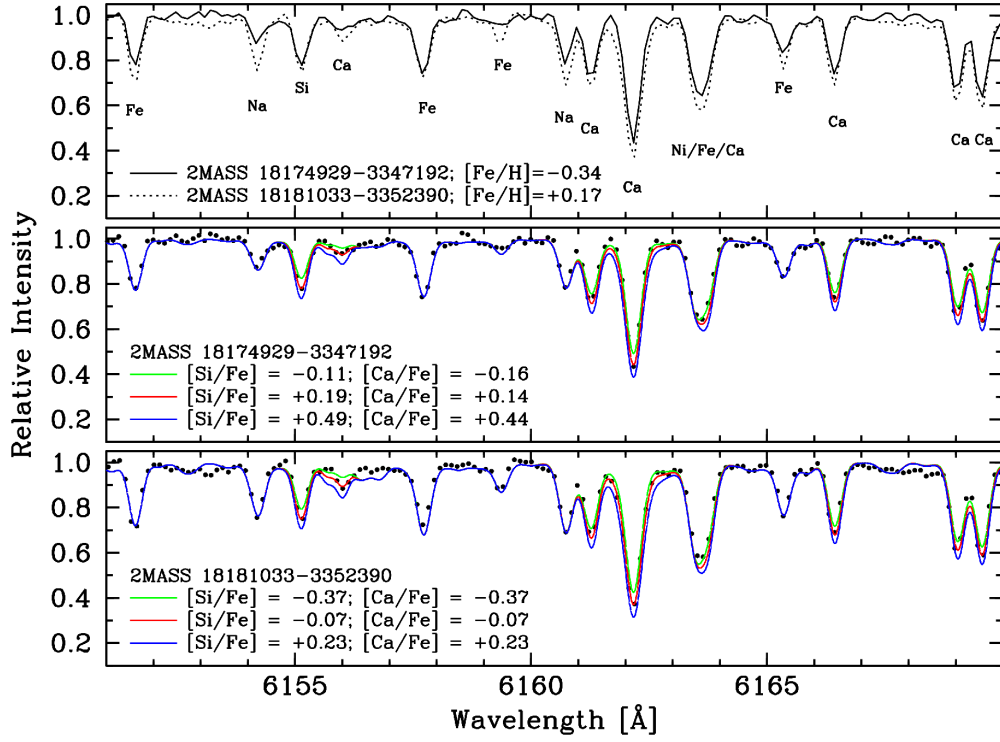


Fig. 3.— The lines and symbols are the same as in Figure 2, but the spectra shown here are from the foreground red clump sample ($T_{\text{eff}} \approx 4900$ K).

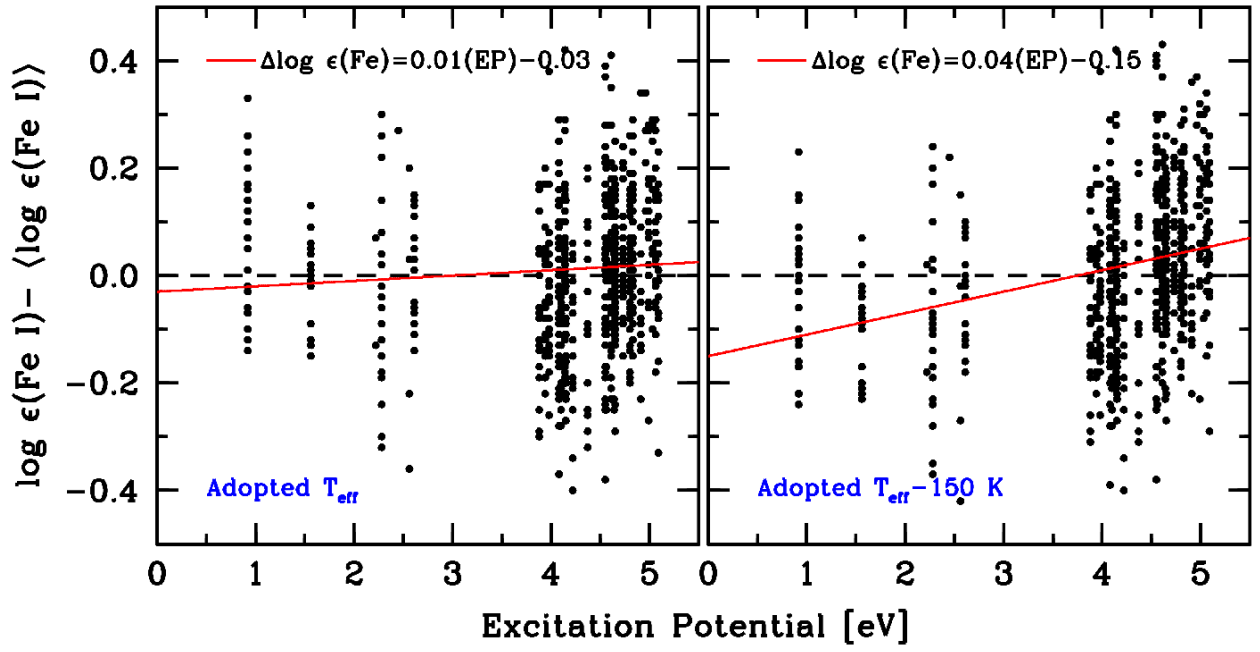


Fig. 4.— The left panel shows $\log \epsilon(\text{Fe I}) - \langle \log \epsilon(\text{Fe I}) \rangle$ versus excitation potential for all lines used in the red clump stars and for our adopted T_{eff} values. The right panel shows how the trend changes when the temperatures are systematically lowered by 150 K. In both panels the solid red line indicates the least-squares fit to the data.

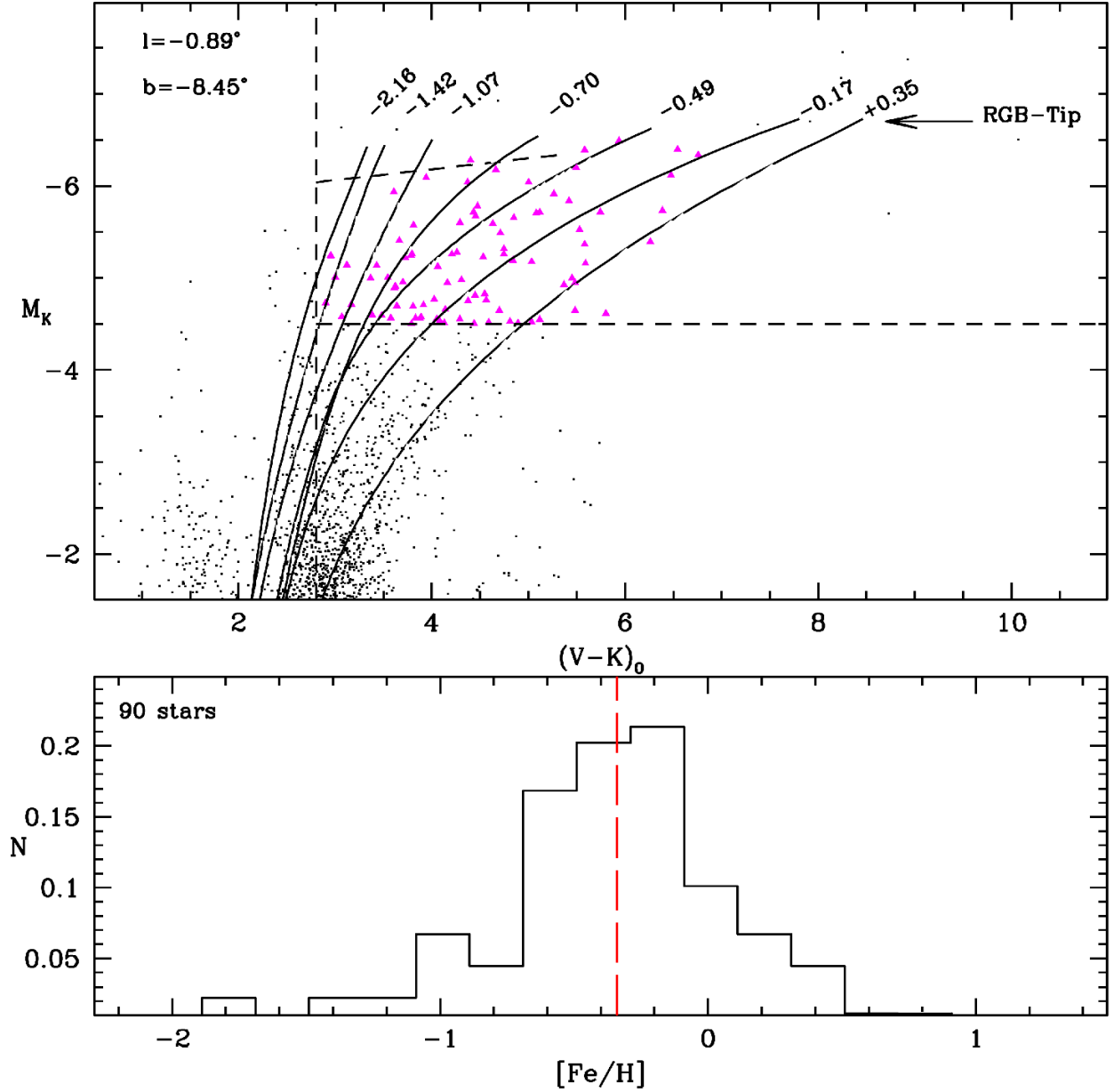


Fig. 5.— The top panel shows the color-magnitude diagram of the bulge field located at $(l,b)=(-0.89^\circ, -8.45^\circ)$ in the absolute plane, with the empirical RGB templates overplotted. The filled magenta triangles indicate the stars inside the dashed box used to derive the photometric metallicity distribution function. The bottom panel shows the derived metallicity distribution function with a bin size of 0.2 dex, and the dashed red line designates the median $[Fe/H]=-0.34$.

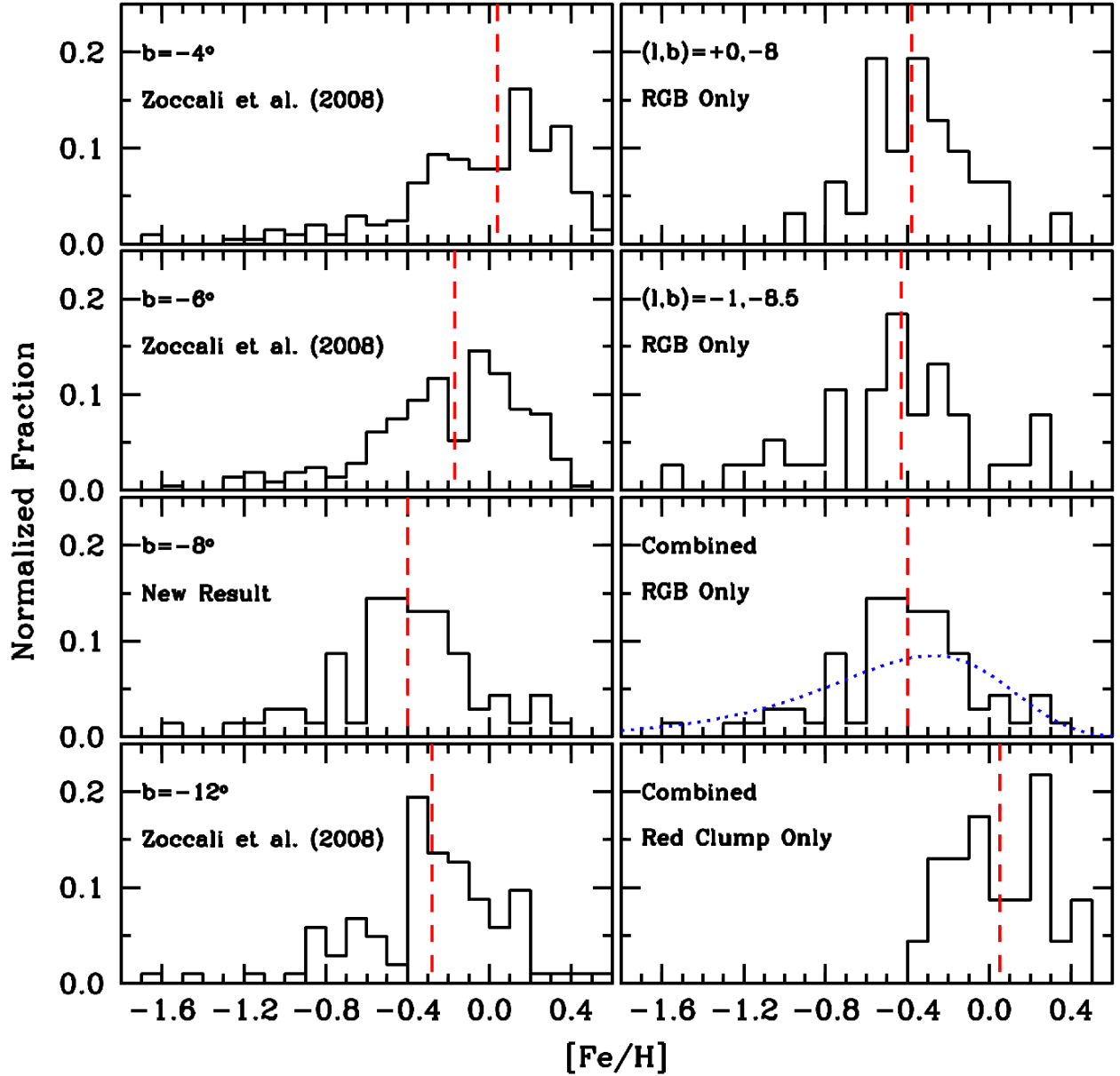


Fig. 6.— Spectroscopic metallicity distribution functions of multiple bulge fields in 0.1 dex bins. For all panels the dashed red line designates the median $[\text{Fe}/\text{H}]$ value. The left panels compare the metallicity distribution functions of Zoccali et al. (2008) to our combined spectroscopic data at $b = -8^\circ$ and $b = -8.5^\circ$. The right panels show the spectroscopic metallicity distribution functions for our two fields. The dotted blue line shows the result of a one-zone, simple model calculation with a yield of $z = 0.0105$. Note that the area under the model curve has been scaled to equal the area under the data histogram.

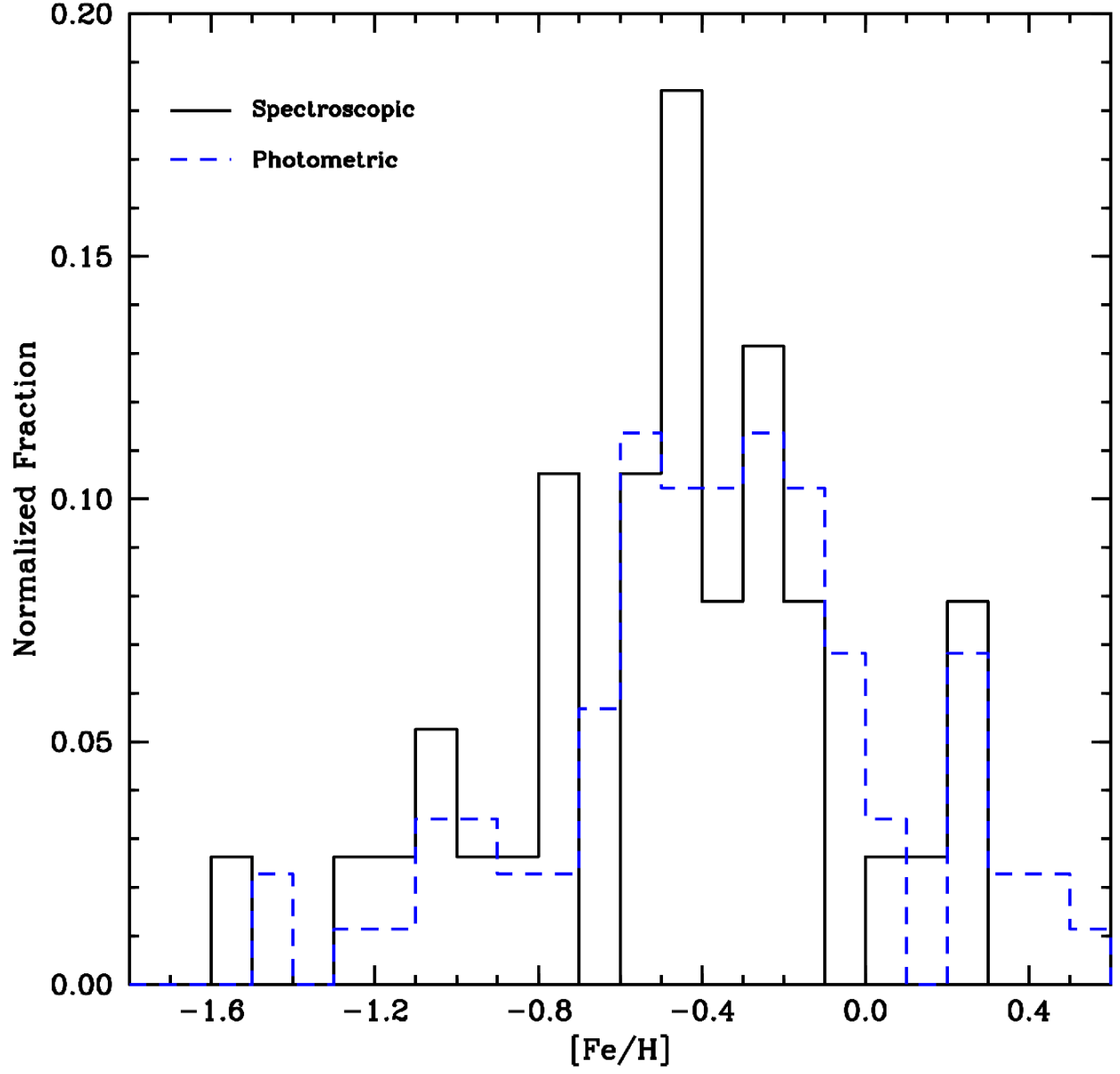


Fig. 7.— Comparison of the metallicity distribution functions determined from spectroscopy (solid black line) and photometry (dashed blue line) in 0.1 dex bins. The spectroscopic and photometric median $[\text{Fe}/\text{H}]$ values are -0.41 and -0.34 , respectively.

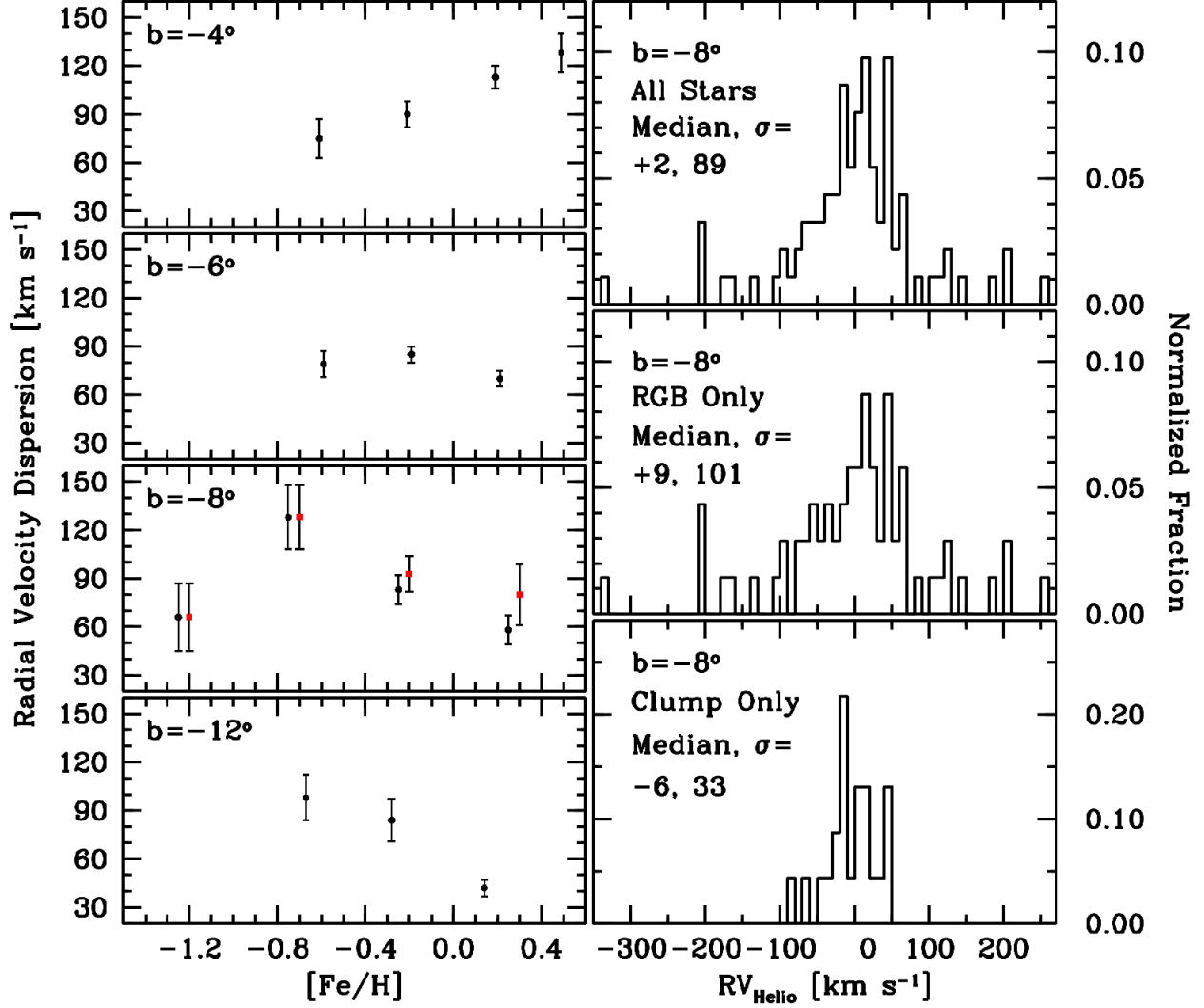


Fig. 8.— The left panels show the measured radial velocity dispersion as a function of metallicity along the bulge minor axis at $b = -4^\circ$, -6° , -8° , and -12° . The $b = -8^\circ$ data are from this study (0.5 dex [Fe/H] bins), and the other fields were taken from Babusiaux et al. (2010; 0.4 dex bins). In the $b = -8^\circ$ panel the filled black circles represent the radial velocity dispersion when the full sample is taken into account, and the filled red squares represent the radial velocity dispersion when only the RGB stars are used. The histograms in the right panels illustrate the radial velocity distribution at $b = -8^\circ$ with the full sample (top panel), the RGB stars only (middle panel), and the foreground red clump stars only (bottom panel) in 10 km s⁻¹ bins.

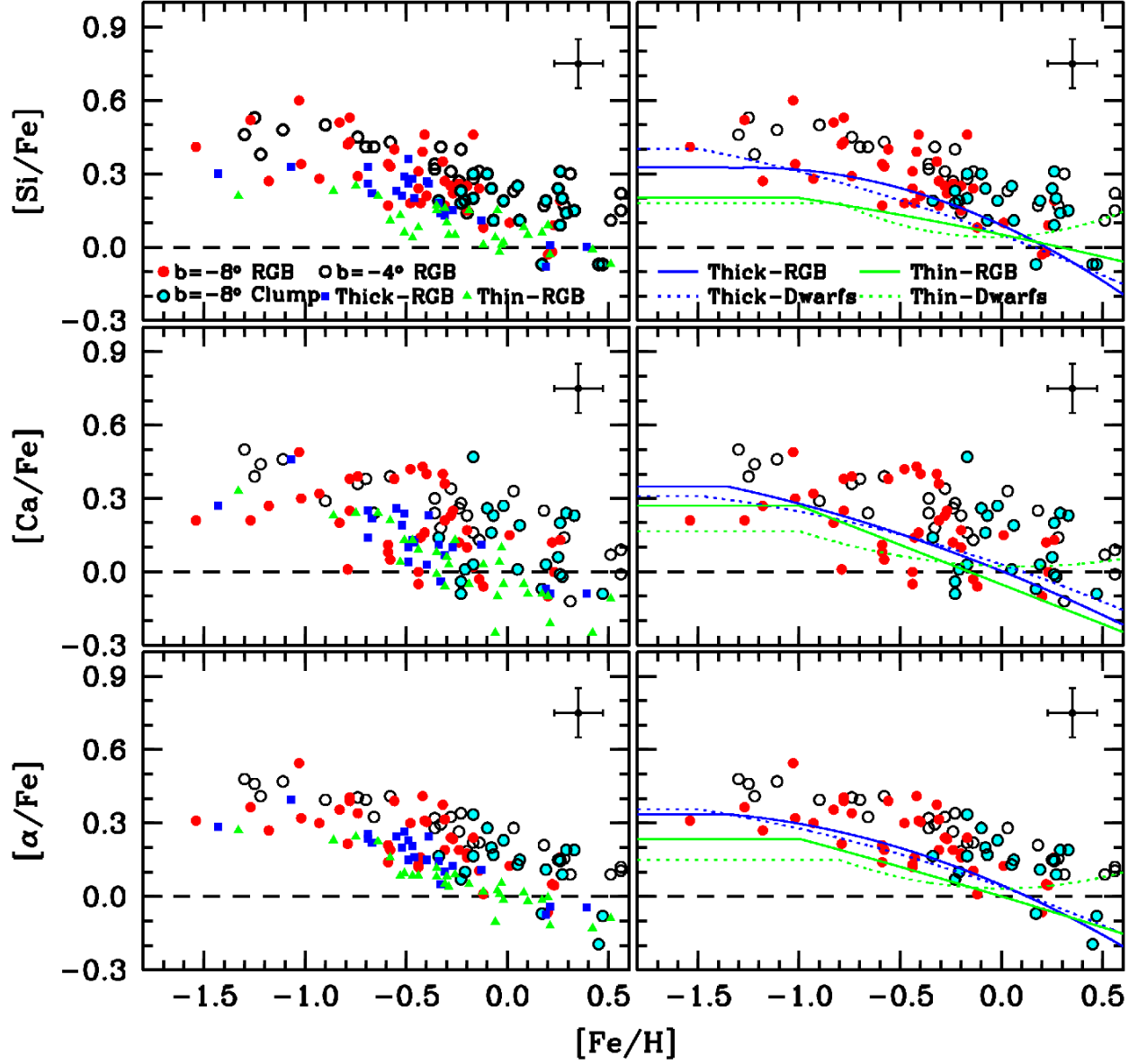


Fig. 9.— The distribution of $[\text{Si}/\text{Fe}]$, $[\text{Ca}/\text{Fe}]$, and $[\alpha/\text{Fe}]$ abundances as a function of $[\text{Fe}/\text{H}]$. The $b = -4^\circ$ data are from Fulbright et al. (2007; AODFNEW only), and the thick/thin disk giant data are from Alves-Brito et al. (2010; Kurucz model atmospheres). The right panels show least squares fits to the literature thin and thick disk data for both giants (solid lines) and dwarfs (dotted lines). The dwarf data were compiled from Fulbright et al. 2000, Bensby et al. (2003; 2005), and Reddy et al. (2003; 2006).

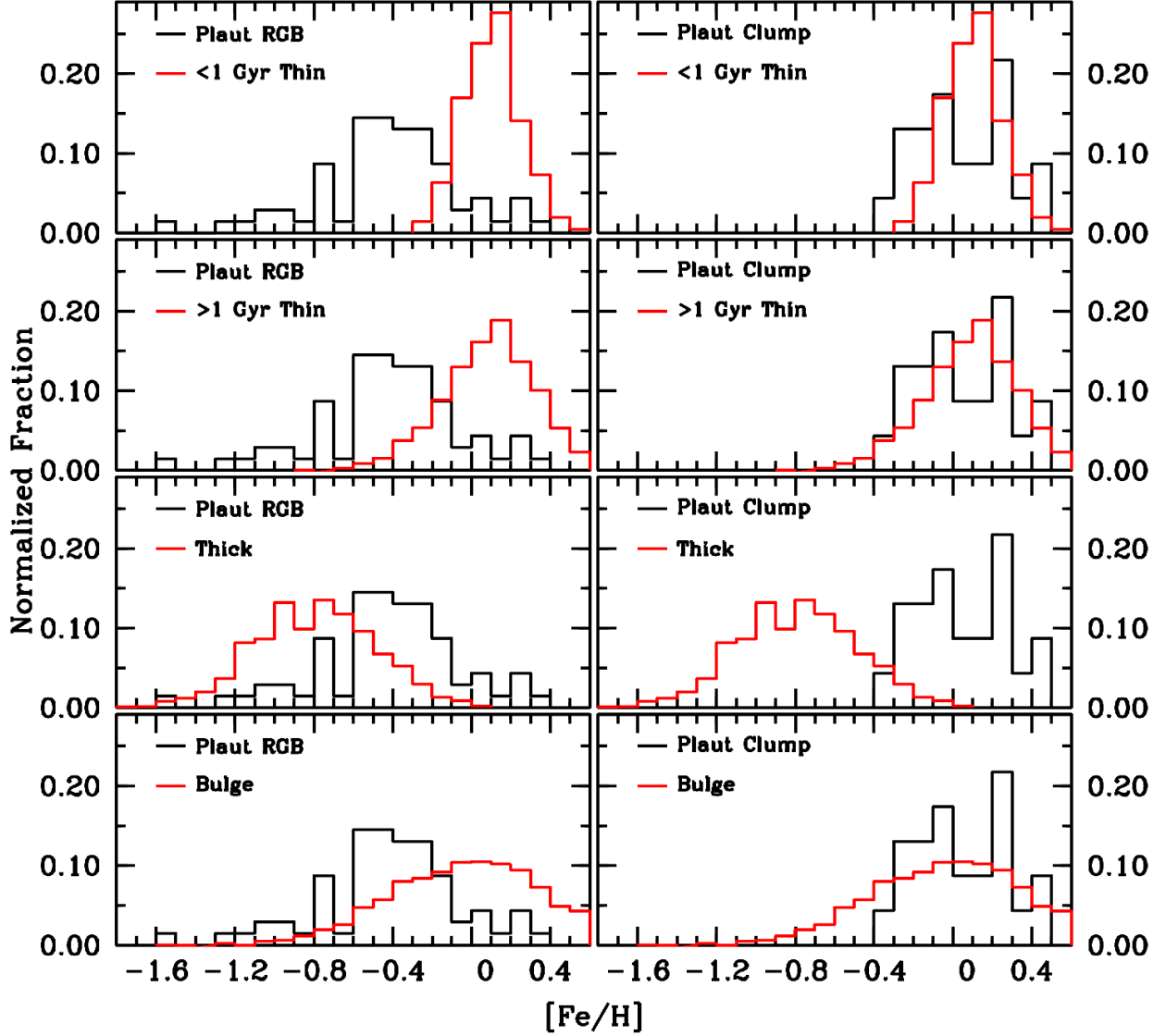


Fig. 10.— Histograms of our observed $[\text{Fe}/\text{H}]$ distributions (solid black lines) versus those predicted for the young (<1 Gyr) thin disk, old (>1 Gyr) thin disk, thick disk, and bulge by the Besancon model (solid red lines). The left panels compare our RGB sample to the model and the right panels compare our red clump sample to the model.

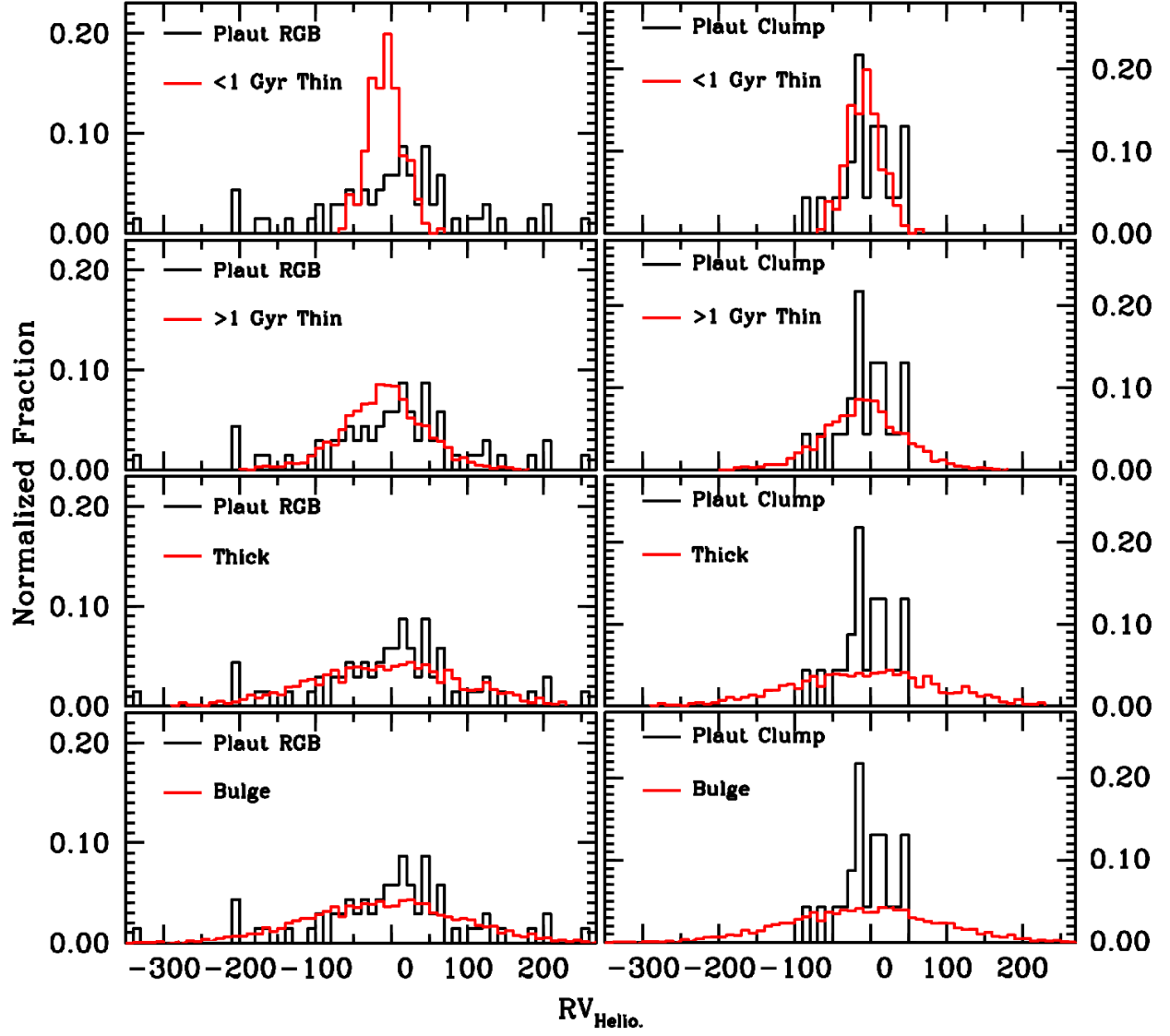


Fig. 11.— Similar to Figure 10 but showing the radial velocity distributions.

Table 1. Program Star Parameters and Results

Star 2MASS	V	J	K _s	T _{eff} (K)	log g (cgs)	[Fe/H]	V _t (km s ⁻¹)	[Si/Fe]	[Ca/Fe]	RV _{Helio.} (km s ⁻¹)	RGB/Field ^a
18174532–3353235	13.957	11.686	10.955	4540	1.45	–1.54	1.65	+0.41	+0.21	–16	RGB/1
18182918–3341405	13.813	10.965	10.046	4125	0.95	–1.27	1.60	+0.52	+0.21	+51	RGB/1
18175567–3343063	14.123	11.645	10.852	4425	1.30	–1.18	1.15	+0.27	+0.27	–107	RGB/1
18181521–3352294	13.533	10.951	10.046	4215	1.00	–1.03	1.55	+0.60	+0.49	+30	RGB/1
18182256–3401248	13.265	10.867	10.104	4465	1.10	–1.02	1.15	+0.34	+0.30	+49	RGB/1
18174351–3401412	13.879	11.525	10.756	4450	1.35	–0.93	1.25	+0.28	+0.32	+2	RGB/1
18182675–3248295	13.870	11.442	10.593	4435	1.25	–0.93	1.95	–36	RGB/2
18172965–3402573	14.403	11.755	10.863	4155	1.35	–0.83	1.80	+0.51	+0.20	+23	RGB/1
18183521–3344124	14.451	11.687	10.785	4150	1.25	–0.79	1.85	+0.42	+0.01	–25	RGB/1
18181435–3350275	13.786	11.356	10.497	4340	1.20	–0.78	1.25	+0.43	+0.38	+2	RGB/1
18183876–3403092	14.120	11.255	10.205	4000	1.05	–0.78	1.80	+0.53	+0.25	+12	RGB/1
18175670–3246550	14.290	11.687	10.742	4290	1.30	–0.76	1.70	+66	RGB/2
18174304–3357006	13.662	10.940	9.980	4090	1.00	–0.74	1.45	+0.29	+0.39	+209	RGB/1
18182636–3253267	13.790	11.361	10.538	4445	1.25	–0.71	1.65	–331	RGB/2
18173757–3256075	14.380	11.992	11.136	4560	1.50	–0.60	0.95	+208	RGB/2
18180831–3405309	13.601	10.859	9.906	4100	1.00	–0.59	1.95	+0.34	+0.08	–95	RGB/1
18180550–3407117	13.963	11.423	10.629	4335	1.25	–0.59	1.45	+0.17	+0.11	–96	RGB/1
18185079–3259346	14.010	11.179	10.141	4055	1.05	–0.59	1.90	+10	RGB/2
18174941–3353025	14.329	11.822	10.968	4275	1.40	–0.58	1.95	+0.33	+0.05	–74	RGB/1
18184795–3257096	14.130	11.671	10.765	4360	1.35	–0.58	1.75	+45	RGB/2
18174742–3348098	14.710	11.984	11.082	4130	1.45	–0.56	1.45	+0.40	+0.38	–18	RGB/1
18185907–3249511	14.360	11.745	10.828	4255	1.35	–0.55	1.85	–77	RGB/2
18184583–3240045	14.180	11.911	11.046	4540	1.45	–0.53	1.05	+6	RGB/2
18180303–3256322	14.350	11.639	10.621	4150	1.25	–0.52	2.05	+184	RGB/2
18183679–3251454	14.170	11.246	10.234	4025	1.10	–0.51	2.00	–210	RGB/2
18181929–3404128	13.729	10.825	9.852	4020	0.90	–0.48	1.30	+0.18	+0.42	+61	RGB/1
18185744–3247526	14.010	11.428	10.510	4275	1.20	–0.46	1.85	+63	RGB/2
18181512–3353545	14.463	11.895	11.067	4270	1.45	–0.44	1.65	+0.24	+0.00	+117	RGB/1
18183802–3355441	13.983	11.446	10.639	4325	1.25	–0.44	1.75	+0.31	–0.05	–58	RGB/1
18174303–3355118	14.265	11.708	10.813	4220	1.30	–0.43	1.60	+0.18	+0.14	–29	RGB/1
18181659–3252450	14.440	12.046	11.199	4465	1.85	–0.43	2.15	–179	RGB/2
18182470–3342166	14.069	11.284	10.353	4145	1.10	–0.42	1.60	+0.39	+0.43	+44	RGB/1
18180285–3342004	14.570	11.754	10.835	4140	1.30	–0.41	1.45	+0.46	+0.16	+27	RGB/1
18181783–3300021	14.200	11.743	10.890	4410	1.40	–0.41	1.15	+50	RGB/2
18174935–3404217	13.777	11.340	10.523	4360	1.25	–0.40	1.70	+0.21	+0.40	–38	RGB/1
18180218–3241380	14.410	12.243	11.397	4665	2.00	–0.39	1.95	+45	RGB/2
18173180–3300124	13.960	11.183	10.181	4200	1.10	–0.38	1.70	+122	RGB/2
18182720–3254318	14.280	11.699	10.812	4290	1.35	–0.38	1.30	+254	RGB/2
18185164–3243594	14.280	12.030	11.219	4600	1.95	–0.35	1.60	+28	RGB/2
18174929–3347192	14.046	12.006	11.362	4875	2.35	–0.34	1.40	+0.19	+0.14	+42	Clump/1
18183604–3342349	13.431	10.573	9.649	4105	0.80	–0.32	1.90	+0.35	+0.40	–59	RGB/1
18183644–3254249	14.390	11.684	10.712	4160	1.30	–0.32	1.55	–138	RGB/2
18180562–3346548	14.293	11.638	10.782	4220	1.30	–0.31	1.75	+0.27	+0.36	+41	RGB/1
18173554–3405009	13.674	11.528	10.772	4625	2.10	–0.31	1.60	+0.17	+0.21	+81	RGB/1
18185946–3240274	13.960	11.344	10.322	4200	1.15	–0.31	1.50	+36	RGB/2

Table 1—Continued

Star 2MASS	V	J	K _s	T _{eff} (K)	log g (cgs)	[Fe/H]	V _t (km s ^{−1})	[Si/Fe]	[Ca/Fe]	RV _{Helio.} (km s ^{−1})	RGB/Field ^a
18173180–3349197	14.328	11.464	10.494	4005	1.15	−0.28	1.25	+0.25	+0.23	+17	RGB/1
18181924–3350222	14.360	11.761	10.887	4215	1.35	−0.27	1.55	+0.22	+0.25	−8	RGB/1
18182065–3248452	14.200	11.567	10.636	4240	1.25	−0.27	2.10	−209	RGB/2
18175593–3400000	14.053	11.380	10.479	4160	1.20	−0.24	1.40	+0.26	+0.12	+14	RGB/1
18182089–3348425	14.284	12.129	11.428	4700	2.15	−0.23	1.45	+0.23	−0.09	−43	Clump/1
18175546–3404103	12.960	11.012	10.351	4950	2.40	−0.23	1.40	+0.18	−0.04	−61	Clump/1
18174688–3257530	14.260	11.981	11.170	4665	2.00	−0.22	1.80	+11	RGB/2
18174798–3359361	13.733	11.721	11.038	4830	2.30	−0.21	1.75	+0.19	+0.01	−11	Clump/1
18184297–3248086	14.300	11.603	10.622	4165	1.25	−0.21	1.35	+123	RGB/2
18180979–3351416	13.107	10.679	9.832	4350	1.65	−0.20	1.70	+0.25	+0.10	+19	RGB/1
18182430–3352453	13.900	11.163	10.265	4130	1.05	−0.20	1.40	+0.15	+0.17	+22	RGB/1
18182494–3250309	14.260	12.117	11.241	4650	2.00	−0.20	1.35	−8	RGB/2
18173251–3354539	14.271	12.033	11.304	4565	1.85	−0.17	2.10	+0.46	+0.02	−6	RGB/1
18181710–3401088	14.395	12.342	11.747	4940	2.40	−0.17	1.45	+0.20	+0.47	+0	Clump/1
18182553–3349465	14.281	12.094	11.383	4660	2.00	−0.17	1.75	+0.30	+0.03	+35	Clump/1
18180991–3403206	13.839	11.327	10.517	4345	1.80	−0.14	1.75	+0.24	−0.03	+62	RGB/1
18184496–3256146	14.160	11.597	10.674	4275	1.30	−0.14	2.05	−163	RGB/2
18184867–3242133	13.930	11.445	10.542	4345	1.25	−0.13	1.90	−44	RGB/2
18180301–3405313	13.896	11.011	10.073	4040	1.00	−0.12	2.05	+0.08	−0.06	−53	RGB/1
18174900–3247128	14.450	11.523	10.468	4070	1.15	−0.11	2.30	+41	RGB/2
18180502–3355071	13.877	11.742	11.049	4715	2.35	−0.10	1.60	+0.30	+0.26	+44	Clump/1
18182740–3356447	14.387	12.172	11.505	4690	2.35	−0.09	1.55	+11	Clump/1
18182457–3344533	14.158	11.823	11.055	4530	2.10	−0.08	1.90	+0.24	+0.15	−15	Clump/1
18182612–3353431	14.319	12.283	11.625	4860	2.40	−0.07	1.65	+0.11	+0.23	−23	Clump/1
18174386–3244555	13.850	11.113	10.114	4200	1.35	−0.07	1.90	+148	RGB/2
18172979–3401118	13.507	11.507	10.846	4860	2.40	−0.02	1.40	+0.19	+0.27	+25	Clump/1
18174571–3259300	14.320	12.053	11.288	4720	2.05	+0.00	1.35	+101	RGB/2
18183930–3353425	14.466	11.833	10.936	4200	1.40	+0.01	1.75	+0.10	+0.15	−66	RGB/1
18181293–3240588	14.070	11.752	10.869	4485	2.00	+0.01	1.30	−200	RGB/2
18174891–3406031	13.505	11.457	10.774	4805	2.40	+0.05	1.70	+0.25	+0.01	−13	Clump/1
18181322–3402227	13.350	11.186	10.507	4740	2.40	+0.06	1.50	+0.11	+0.19	−6	Clump/1
18185947–3246054	14.310	11.425	10.462	4075	1.15	+0.07	1.50	−70	RGB/2
18181033–3352390	13.787	11.793	11.146	4900	2.50	+0.17	1.30	−0.07	−0.07	−18	Clump/1
18174000–3406266	13.254	10.998	10.279	4565	2.30	+0.19	1.85	+0.19	+0.03	−88	Clump/1
18180012–3358096	13.848	11.066	10.144	4090	1.50	+0.20	1.95	−0.03	−0.10	−12	RGB/1
18175652–3347050	13.855	11.183	10.293	4185	1.65	+0.22	1.40	−0.02	+0.12	−2	RGB/1
18182472–3352044	13.858	11.043	10.117	4070	1.45	+0.23	1.80	+0.09	+0.00	+9	RGB/1
18173706–3405569	14.581	12.126	11.409	4405	2.20	+0.25	2.10	+0.24	+0.06	+13	Clump/1
18173994–3358331	14.774	11.962	11.079	4085	1.45	+0.26	1.65	+0.19	+0.13	−41	RGB/1
18182073–3353250	14.509	12.185	11.425	4500	2.30	+0.26	1.55	+0.31	−0.01	+1	Clump/1
18174478–3343290	14.047	11.885	11.224	4785	2.40	+0.26	1.85	+0.09	+0.20	+41	Clump/1
18183369–3352038	13.758	11.523	10.770	4585	2.35	+0.27	1.55	+0.20	−0.02	+10	Clump/1
18183098–3358070	13.511	11.197	10.484	4570	2.35	+0.29	1.65	+0.14	+0.23	+17	Clump/1
18180049–3246462	14.250	11.821	10.956	4460	2.15	+0.32	1.45	−34	RGB/2
18174067–3356000	12.582	10.319	9.577	4540	2.35	+0.33	1.70	+0.15	+0.23	−40	Clump/1

Table 1—Continued

Star 2MASS	V	J	K _s	T _{eff} (K)	log g (cgs)	[Fe/H]	V _t (km s ^{−1})	[Si/Fe]	[Ca/Fe]	RV _{Helio.} (km s ^{−1})	RGB/Field ^a
18173118–3358318	14.225	11.685	10.928	4355	2.00	+0.45	1.85	−0.07	−0.32	−13	Clump/1
18182052–3345251	13.800	11.447	10.669	4505	2.30	+0.47	1.75	−0.07	−0.09	−25	Clump/1

^a“RGB”: probable RGB member; “Clump”: probable red clump member; ‘1’: Field 1 (l=−1°,b=−8.5°); ‘2’: Field 2 (l=0°,b=−8°)

Table 2. Random and Systematic Uncertainties

Star 2MASS	$\sigma_{\text{Rand.}}$ $\log \epsilon(\text{Fe})$	$\sigma_{\text{Sys.}}$ $\log \epsilon(\text{Fe})$	$\sigma_{\text{Rand.}}$ $\log \epsilon(\text{Si})$	$\sigma_{\text{Sys.}}$ $\log \epsilon(\text{Si})$	$\sigma_{\text{Rand.}}$ $\log \epsilon(\text{Ca})$	$\sigma_{\text{Sys.}}$ $\log \epsilon(\text{Ca})$
18174532–3353235	0.15	0.06	0.18	0.04	0.02	0.06
18182918–3341405	0.14	0.06	0.00	0.07	0.11	0.07
18175567–3343063	0.10	0.07	0.06	0.06	0.14	0.06
18181521–3352294	0.11	0.06	0.06	0.09	0.10	0.08
18182256–3401248	0.15	0.07	0.00	0.06	0.00	0.07
18174351–3401412	0.16	0.07	0.00	0.08	0.11	0.07
18182675–3248295	0.18	0.05
18172965–3402573	0.12	0.08	0.06	0.11	0.12	0.08
18183521–3344124	0.13	0.08	0.12	0.10	0.11	0.07
18181435–3350275	0.14	0.06	0.07	0.09	0.14	0.08
18183876–3403092	0.14	0.09	0.06	0.12	0.11	0.09
18175670–3246550	0.21	0.07
18174304–3357006	0.15	0.09	0.09	0.10	0.14	0.09
18182636–3253267	0.16	0.06
18173757–3256075	0.32	0.08
18180831–3405309	0.15	0.07	0.05	0.09	0.09	0.08
18180550–3407117	0.13	0.07	0.08	0.07	0.14	0.08
18185079–3259346	0.24	0.08
18174941–3353025	0.13	0.07	0.13	0.09	0.06	0.07
18184795–3257096	0.24	0.06
18174742–3348098	0.13	0.08	0.08	0.09	0.19	0.10
18185907–3249511	0.08	0.07
18184583–3240045	0.23	0.08
18180303–3256322	0.32	0.07
18183679–3251454	0.18	0.07
18181929–3404128	0.21	0.10	0.00	0.10	0.04	0.10
18185744–3247526	0.15	0.06
18181512–3353545	0.10	0.07	0.07	0.08	0.13	0.08
18183802–3355441	0.11	0.07	0.24	0.08	0.05	0.08
18174303–3355118	0.16	0.08	0.10	0.10	0.14	0.08
18181659–3252450	0.20	0.06
18182470–3342166	0.17	0.09	0.06	0.11	0.02	0.10
18180285–3342004	0.13	0.09	0.00	0.13	0.07	0.10
18181783–3300021	0.17	0.08
18174935–3404217	0.14	0.08	0.01	0.09	0.14	0.08
18180218–3241380	0.17	0.05
18173180–3300124	0.15	0.09
18182720–3254318	0.27	0.09
18185164–3243594	0.21	0.06
18174929–3347192	0.19	0.06	0.05	0.07	0.10	0.07
18183604–3342349	0.15	0.10	0.03	0.12	0.06	0.10
18183644–3254249	0.17	0.10
18180562–3346548	0.14	0.09	0.06	0.11	0.06	0.10
18173554–3405009	0.17	0.06	0.05	0.08	0.00	0.07
18185946–3240274	0.22	0.09

Table 2—Continued

Star 2MASS	$\sigma_{\text{Rand.}}$ $\log \epsilon(\text{Fe})$	$\sigma_{\text{Sys.}}$ $\log \epsilon(\text{Fe})$	$\sigma_{\text{Rand.}}$ $\log \epsilon(\text{Si})$	$\sigma_{\text{Sys.}}$ $\log \epsilon(\text{Si})$	$\sigma_{\text{Rand.}}$ $\log \epsilon(\text{Ca})$	$\sigma_{\text{Sys.}}$ $\log \epsilon(\text{Ca})$
18173180–3349197	0.15	0.12	0.16	0.13	0.12	0.10
18181924–3350222	0.14	0.09	0.20	0.12	0.09	0.10
18182065–3248452	0.17	0.08
18175593–3400000	0.14	0.10	0.12	0.11	0.06	0.10
18182089–3348425	0.16	0.06	0.07	0.09	0.15	0.07
18175546–3404103	0.14	0.06	0.00	0.06	0.10	0.06
18174688–3257530	0.17	0.06
18174798–3359361	0.12	0.06	0.04	0.07	0.00	0.07
18184297–3248086	0.29	0.10
18180979–3351416	0.09	0.08	0.05	0.10	0.10	0.08
18182430–3352453	0.15	0.10	0.07	0.11	0.09	0.10
18182494–3250309	0.29	0.07
18173251–3354539	0.10	0.06	0.09	0.10	0.12	0.07
18181710–3401088	0.15	0.06	0.14	0.07	0.15	0.08
18182553–3349465	0.21	0.06	0.04	0.08	0.01	0.07
18180991–3403206	0.19	0.08	0.09	0.09	0.06	0.08
18184496–3256146	0.14	0.08
18184867–3242133	0.18	0.07
18180301–3405313	0.13	0.09	0.08	0.11	0.02	0.09
18174900–3247128	0.16	0.08
18180502–3355071	0.12	0.07	0.10	0.09	0.09	0.07
18182740–3356447	0.17	0.07	0.00	...	0.00	...
18182457–3344533	0.16	0.06	0.05	0.08	0.15	0.08
18182612–3353431	0.12	0.07	0.09	0.07	0.11	0.07
18174386–3244555	0.21	0.08
18172979–3401118	0.15	0.07	0.04	0.08	0.13	0.09
18174571–3259300	0.19	0.07
18183930–3353425	0.17	0.09	0.11	0.09	0.14	0.10
18181293–3240588	0.10	0.08
18174891–3406031	0.12	0.07	0.07	0.08	0.10	0.07
18181322–3402227	0.11	0.08	0.11	0.08	0.00	0.08
18185947–3246054	0.27	0.11
18181033–3352390	0.15	0.07	0.07	0.08	0.12	0.08
18174000–3406266	0.12	0.09	0.03	0.11	0.05	0.09
18180012–3358096	0.13	0.12	0.15	0.13	0.00	0.09
18175652–3347050	0.12	0.11	0.10	0.12	0.04	0.11
18182472–3352044	0.19	0.12	0.04	0.13	0.10	0.11
18173706–3405569	0.18	0.09	0.07	0.11	0.09	0.08
18173994–3358331	0.16	0.11	0.00	0.12	0.11	0.12
18182073–3353250	0.15	0.10	0.09	0.12	0.14	0.09
18174478–3343290	0.14	0.07	0.14	0.09	0.06	0.08
18183369–3352038	0.14	0.09	0.08	0.10	0.08	0.10
18183098–3358070	0.12	0.09	0.04	0.09	0.10	0.09
18180049–3246462	0.20	0.10
18174067–3356000	0.15	0.08	0.03	0.09	0.10	0.09

Table 2—Continued

Star 2MASS	$\sigma_{\text{Rand.}}$ $\log \epsilon(\text{Fe})$	$\sigma_{\text{Sys.}}$ $\log \epsilon(\text{Fe})$	$\sigma_{\text{Rand.}}$ $\log \epsilon(\text{Si})$	$\sigma_{\text{Sys.}}$ $\log \epsilon(\text{Si})$	$\sigma_{\text{Rand.}}$ $\log \epsilon(\text{Ca})$	$\sigma_{\text{Sys.}}$ $\log \epsilon(\text{Ca})$
18173118–3358318	0.15	0.09	0.06	0.09	0.03	0.09
18182052–3345251	0.17	0.09	0.05	0.08	0.02	0.09